Universidade da Beira Interior
Departamento de Ciências Aeroespaciais

A Preliminary Study on Passive and Active Flutter Suppression Concepts for Aeronautical Components

Luís António Dias Paulo

Submitted to the University of Beira Interior in partial fulfillment of the requirements for the Degree of Master of Science of
Aeronautical Engineering

Covilhã, July 2009

Acknowledgments

This work would not have been possible without the valuable knowledge, guidance, support and encouragement of Dr. Pedro Gamboa, under whose supervision I chose this topic and began the thesis.

I am also grateful to Dr. José Miguel Silva, my co-advisor, for his careful advices and for providing me motivation during the research and graduation.

Finally, I would like to dedicate this thesis to my parents, my sister and Cláudia. Thank you for your continued love, encouragement and support. Without you, I simply would not be who and where I am today.

Abstract

The scope of this work is to study computationally both passive and active flutter suppression characteristics of a cantilever cork agglomerate core sandwich with CFRP facings and an aluminum plate, the latter through the application of piezoelectric patches, respectively. Recently, cork agglomerates have been gaining an increasing interest from the aerospace industry due to their good thermal and acoustic insulation capabilities. In addition, cork based materials intrinsically have excellent vibration suppression properties, which suggest that the combination of cork with high performance composites (such as CFRPs) may lead to high specific strength materials with improved damping characteristics suitable for flutter prevention.

Sandwich specimens were modeled using commercially available software ANSYS® and a demo version of ZAERO® software for the determination of the flutter speed and related frequencies. ANSYS® piezoelectric modeling and transient analysis capabilities were used for the active vibration study. Specimen aspect ratio and thickness were chosen as a function of wind tunnel maximum speed for further experimental tests. Results were compared with conventional CFRP and aluminum plates.

It was demonstrated that a cork agglomerate core sandwich with CFRP facings can act as a natural flutter suppresser which allows the reduction of the wing weight for a given flight envelope and that the application of piezoelectric actuators is a valuable aeroelastic control concept. An increase of about 20% in flutter speed was achieved using actuated piezoelectric devices. The main goal remains in investigating higher strain smart materials and control strategies, since these improvements are only possible in small structures.

Keywords: Flutter, Aeroelasticity, Sandwich, Cork, Piezoelectric, Control

Resumo

O objectivo deste trabalho é o estudo computacional de soluções de supressão de flutter, passiva e activa, através de uma sandwich com núcleo de aglomerado de cortiça e faces de carbono-epoxy e de uma placa de alumínio, esta última através de actuadores piezoeléctricos, respectivamente. Recentemente, os aglomerados de cortiça têm ganho um interesse crescente por parte da indústria aeronáutica devido às suas propriedades de isolamento térmico e acústico. Além disso, os materiais à base de cortiça têm intrinsecamente excelentes propriedades anti-vibráticas, o que sugere que a sua combinação com materiais de alto desempenho (como o carbono-epoxy) pode levar a materiais de resistência específica elevada e com características de amortecimento melhoradas, adequados à prevenção do flutter.

A sandwich foi modelada usando o software de elementos finitos ANSYS® e uma versão de demonstração do ZAERO® para a determinação da velocidade de flutter e respectiva frequência. Por sua vez, as capacidades de modelação piezoeléctrica e transiente do ANSYS® foram usadas para o estudo do controlo de vibração activa. A razão de aspecto das placas foi escolhida em função da velocidade máxima do túnel de vento, para posteriores testes experimentais. Os resultados foram comparados com placas de alumínio e carbono-epoxy convencionais.

Foi demonstrado que a sandwich com núcleo de aglomerado de cortiça pode actuar como um supressor natural de flutter que permite uma redução do peso da estrutura para um dado envelope de voo. No que concerne ao controlo activo, a aplicação de actuadores piezoeléctricos é um conceito de controlo aeroelástico valioso que permitiu, neste estudo, um aumento de 20% na velocidade de flutter. No entanto, o principal objectivo permanece em investigar estratégias de controlo e materiais de características piezoeléctricas com capacidade de induzir maiores extensões a custo de uma menor potência.

Palavras-Chave: Flutter, Aeroelasticidade, Sandwich, Cortiça, Piezoeléctrico, Controlo

Contents

List of Figures

List of Tables

Nomenclature

$[M]$	Mass matrix
$[C]$	Damping matrix
$[K]$	Stiffness matrix
$\{D\}$	Vector of nodal degrees of freedom
$\{\bar{D}\}$	Variation of nodal displacements from static equilibrium
$\{R_{ext}\}$	Vector of externally applied forces
Ω	Natural frequency of vibration or oscillation
V_f	Flutter speed
ρ_0	Air density at sea level
r_e	Elastic axis aft location from leading edge at 70% half wing span relative to plate chord
c	Plate/ceramic width
b	Plate/ceramic length
r_s	Mass axis aft location from leading edge at 70% half wing span relative to plate chord
c_i	Plate chord at center line
c_m	Mean chord
Λ	Aspect ratio
k_T	Plate torsion stiffness
k_B	Plate flexural stiffness
F	Plate area
σ	Density ratio

m_F	Plate mass
b	Plate length
s	Vertical displacement at 70% half span
φ	Rotational displacement at 70% half span
P	Point load
M_T	Torsion moment
M_∞	Freestream Mach number
Φ	Total velocity potential
ϕ_0	Steady potential
ϕ_1	Unsteady potential
ϕ	Reduced frequency domain potential
C_p	Unsteady pressure coefficient
q_∞	Freestream dynamic pressure
$[NIC]$	Normal velocity influence coefficient matrix
$\{h\}$	Structural deformation at each aerodynamic box
$\{L_h\}$	Resultant aerodynamic force vector at each aerodynamic box
$[T]$	Spline matrix
$[\Phi]$	Modal transformation matrix
[AIC]	Aerodynamic influence coefficient matrix
$[\bar{B}]$	Aerodynamic influence coefficient calculation matrix
$[\bar{F}]$	Aerodynamic influence coefficient calculation matrix
$[\bar{D}]$	Aerodynamic influence coefficient calculation matrix or electric displacement
q	Generalized coordinates or total electric charge
F_a	Aerodynamic force

k	Reduced frequency
Q(ik)	Aerodynamic influence coefficient matrix in Laplace domain
σ	Stress vector
ε	Strain vector
E	Vector of applied electric field or Young Modulus
ξ	Permittivity
d	Matrix of piezoelectric strain constants
S	Matrix of compliance coefficients or sensor surface area
e	Matrix of piezoelectric stress coefficients
V	Electric potential
G_c	Gain of current amplifier
i(t)	Current of the sensor
δ	Logarithmic decrement
α and β	Rayleigh damping coefficients
ζ	Damping ratio
T1, T2, T3	Modal Translational Displacement
R1, R2, R3	Modal rotational displacements
G	Shear modulus
t	Plate/Ceramic thickness
y	Tip displacement

Chapter 1 - Introduction

1.1 Motivation

Aeroelastic instabilities are within the factors that most restrict the flight envelope of aircraft. The simultaneous presence of the aerodynamic, inertia, and elastic forces makes it a truly interdisciplinary problem that has been studied since the early days of aviation. The most dangerous aeroelastic phenomenon is flutter, when aerodynamic lifting surfaces suffer a self-excited oscillation that may often be destructive, since the structure absorbs energy from the flow and leads to large amplitude oscillations of the lifting body. Due to its catastrophic nature, it is imperative that the occurrence of flutter on lifting surfaces be suppressed, to avoid failure of the structure due to large deformation. The mission profile of the next generation of Unmanned Air Vehicle (UAV) will lead to a design requirement of an adaptable airframe to best meet the varying flight conditions. It is conceivable that the changes in geometry that occur would also incur aeroelastic instabilities, such as flutter, at points of transition during the mission.

In that regard, several passive solutions like strengthened materials and mass balancing have been developed to prevent this hazardous phenomenon. It is believed that cork based materials may have a contribution in flutter suppression due to its natural damping characteristics. The present study aims at evaluating the feasibility of using a cork agglomerate combined with carbon reinforced plastics (CFRP) in a sandwich structure in order to increase structural eigenvalues and, consequently, critical flutter speed and frequency. The main goal is to reduce the weight of the wing for a given flight envelope without changing dramatically structural strength.

On the other hand, when changes in the structure or in the aerodynamics are not viable for flutter prevention, the use of active materials becomes a good option. Recent investigations confirm the advantages of using adaptive structures for this purpose, the most part combining high performance composite materials with bonded smart actuators, such as piezoelectric materials. When a command signal is applied to the piezoelectric actuators, these will exert control over the damping and stiffness properties of the component. In this study, a computational method based on ANSYS® is used for the active vibration control analysis.

1.2 Objectives

This work will be divided in two distinct tasks. The first objective is to study the feasibility of using a cork based sandwich, with carbon fiber facesheets, as a passive flutter suppresser. To do so, a finite element model of a sandwich rectangular plate will be modeled in ANSYS® and the aerodynamic coupling will be performed using ZAERO® software in order to compute the sandwich flutter speed. The goal is to demonstrate that this type of sandwich can be a viable aeroelastic solution to aircraft components when compared to conventional aluminum and carbon/epoxy plates, since it can allow an increase in flutter speed for a lighter structure.

The second objective is to perform a computational study on active flutter suppression using piezoelectric materials. An aluminum plate with six attached piezoelectric patches will be modeled using ANSYS® piezoelectric analysis capabilities in order to analyze to what extent the piezoelectric actuation affects the rigidity and damping characteristics of the aluminum plate and allows a consequent increment in flutter speed. The goal is to quantify this increment through the decrease of the oscillations amplitude of the excited structure.

1.2 Literature Review

Since its early days, aircraft have suffered the effects of aeroelastic flutter. Flutter is usually the result of coupling between two or more structural modes influenced by unsteady aerodynamics. The rate of damping of the oscillation of the disturbed airfoil first increases when the speed of the flow around the airfoil gradually increases. With further increase of flow speed, however, a point is reached at which the damping rapidly decreases. Below the critical flutter speed, an oscillation can just maintain itself with steady amplitude. At flow speeds above the critical speed, a small disturbance of the airfoil can serve as trigger to initiate an oscillation of great violence. The oscillatory motion of a fluttering cantilever wing has both flexural and torsional components. A rigid airfoil constrained as to have only the flexural degrees of freedom does not flutter. If the airfoil is constrained as to have only the torsional degrees of freedom, it can flutter only if the angle of attack is at or near the stalling angle [1]. The first recorded flutter incident was on a Handley Page 0/400 twin engine biplane bomber in 1916 [2]. The flutter mechanism consisted of a coupling of the fuselage torsion mode with an anti-symmetric elevator rotation mode. But it was only by the early stages of World War II that this problem began to attain a prominent importance. As aircraft speed increased, with little or no increase in load requirements, and in the absence of rational stiffness criteria for design, aircraft designers encoutered a wide variety of problems which we now classify as aeroelastic problems [3].

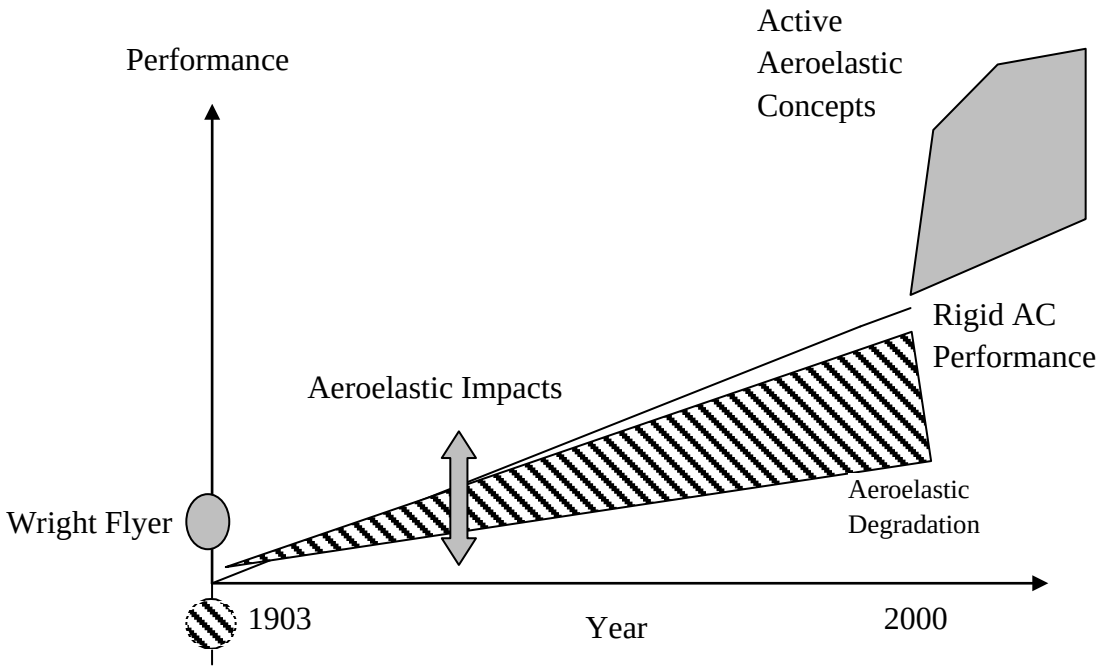

Fig. 1- The impact of aeroelasticity on aircraft performance [4].

The role of aeroelasticity in aircraft performance over the years is depicted in Fig. 1. Its impact is caused mainly because of increasing speed but also by the advent of lighter and more flexible structures like composites.

Passive solutions such as increased structural stiffness, mass balancing, or modified geometry have been used to prevent this hazardous phenomenon. But these approaches resulted in increased weight and cost, and decreased performance [5]. The introduction of composite materials with highly anisotropic directional stiffness properties in the 1970's helped to create aeroelastic tailoring design methods. The progress in aeronautics is intimaly connected to the progress in aeroelasticity and related external stimuli and events. This transition was supported by improved structural analysis and mathematical optimization methods capable of simulating the composition and orientation of the individual material layers that were tailored to minimize the extra amount of structural weight for reducing the impacts from aeroelasticity (Fig. 2) [6].

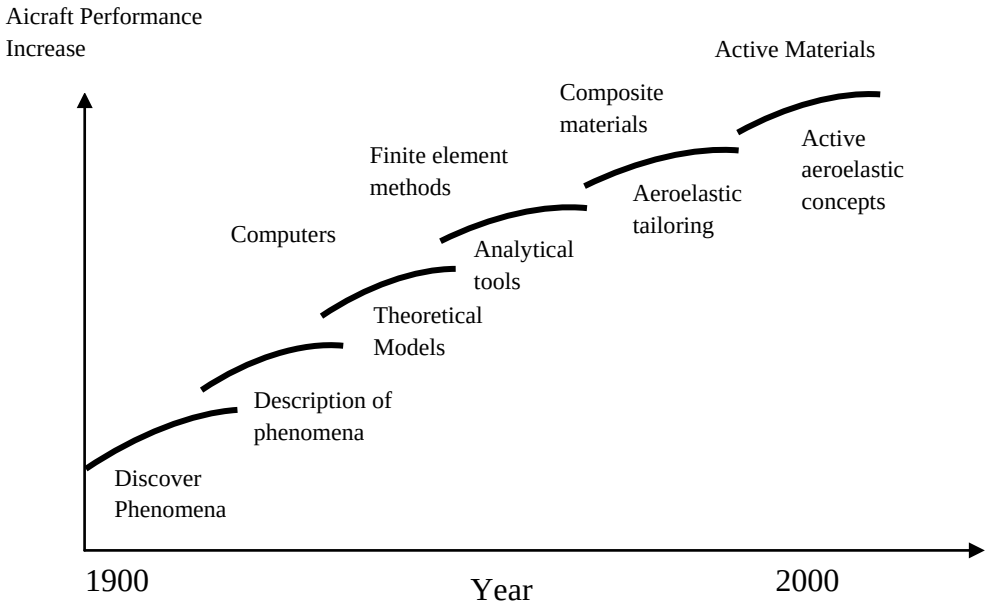

Fig. 2 - Relationship between aircraft performance, advances in aeroelasticity, and external stimuli [4].

Modeling structural dynamics and unsteady aerodynamics has been a difficult task throughout the years. Regarding structural dynamics, the first studies have considered Theodorsen´s structural model. This model represented the wing only by one section in which the bending motion was associated to the vertical displacement and the torsion motion was associated to rotational displacement. However, this model did not give a good representation of the full wing dynamics. With the development of finite element method codes, with quite complete element

libraries, several complex structures began to be simulated using computers. Regarding the unsteady aerodynamics, the first subsonic model used in aeroelastic analyses was provided also by Theodorsen using a typical wing section. This was a potential and two-dimensional model based on the lifting theory for a flat plate [7]. However, several other methods have been developed since then like the vortex–lattice and the doublet–lattice methods where the vortex represents the steady flow and the doublet represents the incremental effect of the oscillation and unsteady motion. This method was used by Heeg in Ref [5].

During World War II the first theoretical writings about sandwich appeared. In the 1950's the development was mainly concentrated on honeycomb materials. Honeycomb was mainly used as a core material in the aircraft industry. However, it had some limitations, for example there were big problems with corrosion.

At the end of the 1950's and during the 1960's different cellular plastics were produced, suitable as core materials. In the beginning, rather soft materials were used because of their insulation properties, for example polystyrene and polyurethane. Later, it was possible to produce harder cellular plastics with higher densities and by that time sandwich became a very useful and flexible concept [8]. Today there is an enormous number of different qualities of cellular plastics as core materials; however, cork agglomerates are arising as potential competitors to conventional plastics not only because of its mechanical properties but also for its eco-friendly characteristics. In this regard, one of the goals of the present work is to evaluate the feasibility of using cork composite sandwiches as a passive flutter suppresser structure.

Recently, cork based composites have been gaining a rising interest from the aerospace industry due to their good thermal and acoustic insulation capabilities [9]. Cork based materials intrinsically have excellent vibration suppression properties [10], which suggest that the combination of cork with high performance composites (such as CFRPs) may lead to high specific strength materials with improved damping characteristics.

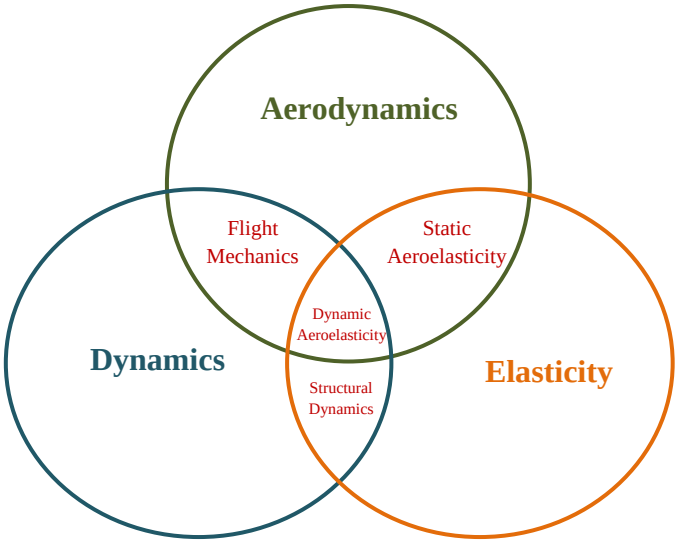

Fig. 3 - Collar´s Aeroelastic Triangle [11].

The aim is to use the sandwich material with maximum efficiency. The two faces are placed at a distance from each other to increase the moment of inertia and, thereby, the rigidity. A comparison can be made with a solid plate. A sandwich plate of the same width and weight as a solid plate has a remarkably higher stiffness because of its higher second moment of area. This will provide an increase in flutter speed for a lighter structure.

However, due to historical passive solution´s drawbacks, active flutter suppression methods have been introduced in aerospace investigation. The well known Collar´s Aeroelastic Triangle, depicted in Fig. 3, has been upgraded to consider the interaction of smart structures as illustrated in Fig. 4. One of the pioneer studies in this matter was the Active Aeroelastic Wing program by NASA. The AAW technology employs wing aeroelastic flexibility for a net benefit through use of multiple leading and trailing edge control surfaces activated by a digital flight control system. At high dynamic pressures, the AAW control surfaces are used as tabs that are deflected into the airstream in a manner that produces favorable wing twist [12]. Though widely used, conventional technologies for active control of flutter and vibrations based on servo-valve/hydraulic actuators have several limitations such as: (1) multiple energy conversions (mechanical, hydraulic, electrical); (2) large number of parts, i.e., potential failure sites and large weight penalty; (3) high vulnerability of the hydraulic pipes network; (4) frequency bandwidth limitations. High performance induced strain actuators are capable of large

forces and up to 0.1% free strain. Its main drawbacks are the very small strokes limited on this inherent capacity on the free induced-strain response (for example, a 100 mm long actuator is capable of a mere 0.1 mm peak-to-peak stroke) [14], especially due to torsional rigidity. This is the main reason why this type of control is not being applied in today´s full scale military or civil aircraft. However, the mission profile of the next generation of UAV will probably lead to a configuration requirement of an adaptable airframe to best meet the varying flight conditions. It is conceivable that the changes in geometry that occur would also incur aeroelastic instabilities, such as flutter, at points of transition during the mission [15].

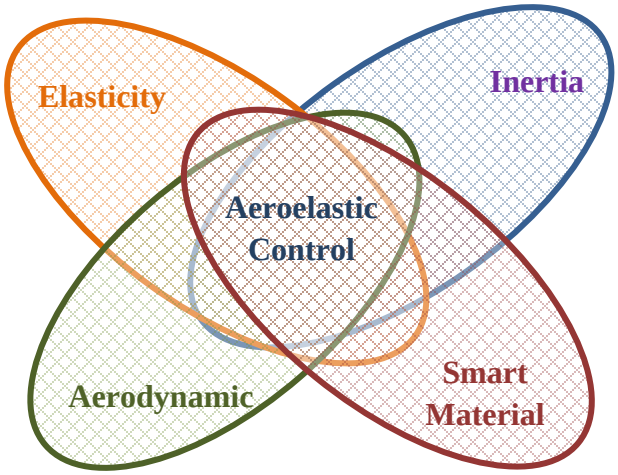

Fig. 4 - Aeroservoelasticity Disciplines [12].

A review on several active aeroelastic control methods for helicopter blades and fixed wing aircraft is presented in Ref. [14]. Besides the already mentioned AAW program, the most remarkable studies on the latter are the PARTI and ACROBAT programs. A 4 ft long semi-span wing model successfully demonstrated flutter suppression and gust loads alleviation in the PARTI program. For these tests, a wing model of a composite plate (graphite epoxy facesheets with aluminum honeycomb core) with 36 piezoelectric wafers surface bonded to each side of the plate were used. Both active aeroelastic control and active/passive shunt damping were investigated. For active aeroelastic control, the power required to achieve effective control-law implementation was monitored. The maximum power consumption to achieve a perfectly controlled structure was found to be a function of material and geometric properties of the piezoelectric actuator and not to depend on the complex system dynamics. The tests proved that

12% increase in flutter dynamic pressure and 75% of gust bending moment are achievable. In the ACROBAT program, the feasibility of using piezoelectric control to alleviate vertical tail buffeting of the F-18 was investigated. The vertical tail was equipped with surface bonded piezoelectric wafer actuators and first bending resonance was increased by as much as 60%.

Although, there have been significant amount of literature reported in the area of active vibration control of flexible structures using smart structures [16,17,24] , only a limited number of research works have been carried out in the field of dynamic aeroelastic control [5,18-23]. A smart structure can be defined as the structure that can sense an external disturbance and respond to that with active control in real time to maintain the mission requirements. Although strain and displacement are usually used as the feedback parameters for the control system, other studies have been performed using pressure sensors at a point in the wing surface [7]. Smart structures consist of highly distributed active devices which are primarily sensors and actuators either embedded or attached to an existing passive structure with integrated process networks [26]. Controllers that can be both classic and modern control schemes, such as proportional-integral-derivative control, lead-lag compensator and linear quadratic regulator, H_2, H_∞ and μ-synthesized are used in active vibration control [21]. The effectiveness of some of these control strategies are compared in [22].

Several aeroservoelastic tools have been developed to couple the structural active vibration control to aerodynamic loading, namely flutter suppression. A short review on aeroeservoelastic computational tools is presented in [23]. ZAERO®, a recently developed aeroelastic code at ZONA Technology can also be used for aeroservoelastic analyses. The code, which is a derivation of the doublet-lattice method, has been validated when the influence of the aerodynamic stores on the aeroelastic instability has been studied using a number of aerodynamic models for the F-16 aircraft configurations, including the isolated wing-tip launcher model, and the whole aircraft with and without stores. A good agreement was shown between the ZONA6 code results and test data. A free demo version of ZAERO® software limited to 40 wing boxes is used in the present study for the flutter speed and frequencies computation.

Among several functional materials, piezoelectric transducers (PZTs) have drawn attention as a possible actuation mechanism for flutter prevention systems because of their simple structure and fast response time. Application of piezoelectric actuation to flutter control of a more realistic wing model was achieved under the piezoceramic aeroelastic response tailoring investigation (PART I) program at NASA Langley research center [5].

Ref. [24] summarizes the development of a piezoelectric-based electromechanical device useful for suppression of vibration and compares several types of piezoelectric actuation that can be used for vibration suppression. There are three piezo-actuator parameters which affect the structural properties as well as the control characteristics: actuator thickness, area and location [25]. Lead zirconate titanate (PZT) piezoceramic is the most common transducer material, and several compositions are available. The basic decision in selecting PZT actuation materials comes down to “hard” versus “soft” compositions, e.g., PZT-4 and PZT-5. Thus, for a larger applied voltage across a given thickness, the PZT-4 compositions can produce as large a strain as the PZT-5 compositions generate at a lower voltage. In addition, the harder materials are less likely to age and are less subject to stress-depoling. The special interest in the development of very low voltage operation has led to forgetfulness in harder compositions despite their benefits. PZT-5A is a good compromise between these two types of composition.

A review on the current architectural trends in amplifying small piezoelectric strains is presented in Ref. [24]. As piezoelectric materials are continually improved and developed, these actuators are finding more applications and their use is becoming more common. Likewise, piezoelectric actuators are becoming more widely available from commercial vendors.

Because the strain levels of traditional piezoelectric (PZT) materials are so small, improvements are continuously being sought. New relaxor ferroelectric crystals (PZN and PMN) have 5 times as much strain energy as conventional piezoceramics. However, reliability, nearly linear response with applied voltage, showing excellent response to the applied electric field over a very large range of frequencies and their relative low cost made piezoelectric materials (PZT´s) the most widely preferred one as collocated both as sensor and actuator. For this reason, BM500 ceramics were chosen for the present work.

Several studies on active flutter suppression report an increment of flutter speed ranging from 6% to 50%. The main challenge remains in finding piezoelectric actuators with a higher stroke, especially to increase torsional control efficiency, and low power requirements.

1.3 Approach/Methodology

Different tasks were accomplished in support of an analysis of the previous described problem. The cantilever plate finite element model was built in ANSYS® Multiphysics in order to obtain the structural eigenvalues and eigenvectors (natural frequencies and mode shapes). This modal data provided by ANSYS® analysis is exported to a file in a free format to be input in the ZAERO® system software.

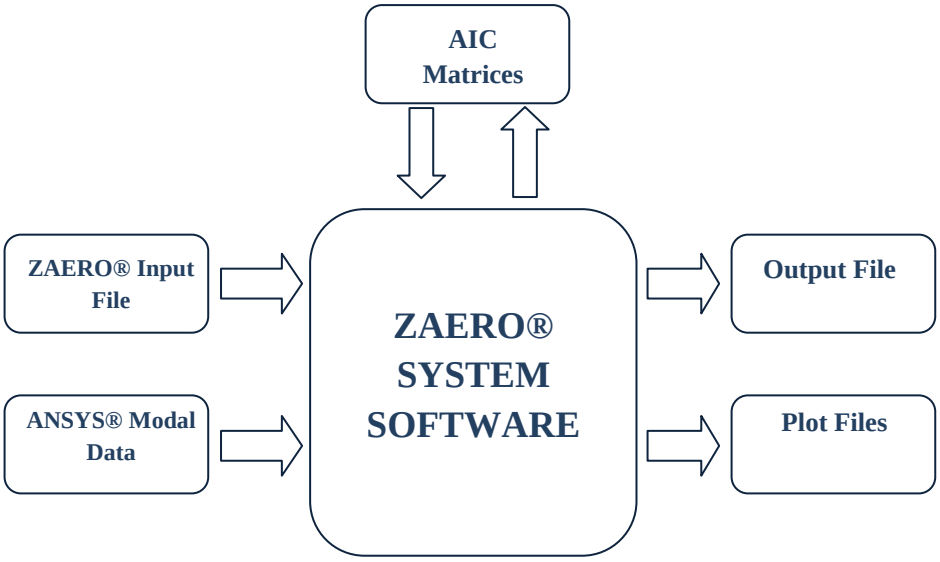

Fig. 5 - ZAERO® System File Processing.

The next step was to build the ZAERO® input file which defines the filename that contains the free vibration modal data from the structural finite element method, type of analysis to be performed, print options for TECPLOT, discipline for analysis, geometry of the aerodynamic model, spline instructions for displacement and force transfer between the structural finite element grid points and the aerodynamic boxes, flight conditions, and other parameters such as reference density, lengths, etc. ZAERO® generates an aerodynamic influence coefficients (AIC) matrix to couple the aerodynamics data to the structural data and provides flutter speed and frequencies in the output file.

An analysis of the higher strain energy density locations for the critical vibration modes was made in ANSYS®. By determining areas of concentrated strain energy, it was possible to choose the general piezoelectric patch placement locations for each node based upon existing finite element model (FEM) nodes. The smart plate model was built in ANSYS® and a static analysis

was performed to estimate the plate tip displacement when a voltage was applied to the PZT actuators.

Finally, active flutter suppression was modeled in ANSYS® APDL through transient analysis. A macro was created in order to apply a voltage to the piezoelectric patches at each different time step so that these exerted a counter force at the plate tip. The scope is to evaluate the decrease of the oscillations amplitude and find an equivalent plate stiffness to introduce in ZAERO®. To do so, different voltage phases were applied according to the displacement of the plate as a function of time.

Chapter 2 – Theoretical Background

2.1 Modal Analysis – Natural Modes of Vibration

The mode shapes at the natural frequencies are of extreme importance, as the deformation of the plate is maximum for these mode shapes [27]. So, in any vibration control methodology, the main aim should be to avoid the natural frequencies at any circumstances. The natural modes of the free vibration for the flat plate are calculated within ANSYS® using modal analysis. The basic principle for this analysis begins with Newton´s second law. For a structure with multiple degrees of freedom, Newton´s second law can be written as

$$[M]\{\ddot{D}\}+[C]\{\dot{D}\}+[K]\{D\}=\{R_{ext}\} \tag{2.1}$$

where $[M]$, $[C]$ and $[K]$ are the mass, damping and stiffness matrices, $\{D\}$ is a generalized vector of the nodal degrees of freedom, and $\{R_{ext}\}$ is a vector of external loads applied to the structure. Since for undamped free vibration the damping is assumed to be zero and there are no externally applied loads, equation (2.1) can be reduced to

$$[M]\{\ddot{D}\}+[K]\{D\}=\{0\} \tag{2.2}$$

Nodal displacements and accelerations associated with the free vibration motion can be written as

$$\{D\}=\{\bar{D}\}\sin\omega t \qquad \{\ddot{D}\}=-\omega^2\{\bar{D}\}\sin\omega t \tag{2.3}$$

where $\{\bar{D}\}$ represents the variation of nodal displacements from static equilibrium. Combination of equations (2.2) and (2.3) yields the eigenproblem for undamped free vibration of a multiple degree of freedom system:

$$\left([K]-\omega^2[M]\{\bar{D}\}\right)=\{0\} \tag{2.4}$$

where ω^2 is an eigenvalue and ω is one of the natural frequencies of vibration. Each eigenvalue and natural frequency will have a corresponding eigenvector. ANSYS® modal analysis provides these natural frequencies of vibration as well as the corresponding mode shapes. Block Lanczos was used for the solver since it performs well when the model consists of poorly shaped shell and solid elements as is the case of the present study.

2.2 Semi – Analytical Method for Flutter Speed Determination

There are several methods that allow computation of flutter speed and frequency. British Gliding Association has developed a relatively simple semi-analytical procedure for glider manufacturers which has proven to be quite reliable for wings with aspect ratio lower than 10 since it has been improved repeatedly [12]. The flutter speed can be computed as:

$$V = \frac{0.94}{\rho_0^{1/2}} \left(\frac{r_e}{r_c^4} \right)^{1/3} \left(\frac{l_i}{l_m} \right) \left(1 + \frac{0.8}{\Lambda} \right) \left(1 + \frac{\Lambda^2}{38} \frac{k_T}{k_B} \right) \left(\frac{k_T}{l_m F} \right)^{1/2} \left(1 + 1.68\sigma \frac{l_m F}{m_F} \right) \tag{2.5}$$

where,

V – Flutter speed (m/s)

ρ_0 – Air density at sea level (kg/m^3)

r_e – Elastic axis aft location from leading edge at 70% half wing span relative to plate chord (m)

r_s - Mass axis aft location from leading edge at 70% half wing span relative to plate chord (m)

c_i – Plate chord at center line (m)

c_m – Mean chord (m)

Λ – Aspect ratio

k_T – Plate torsion stiffness (N/rad)

k_B – Plate flexural stiffness (N.m)

F – Plate area (m^2)

σ – Density ratio

m_F – Plate mass (kg)

b – Plate span (m)s – Vertical displacement at 70% half span (m)

φ – Rotational displacement at 70% half span (rad)

P – Load (N)

M_T – Torsion Moment (N.m)

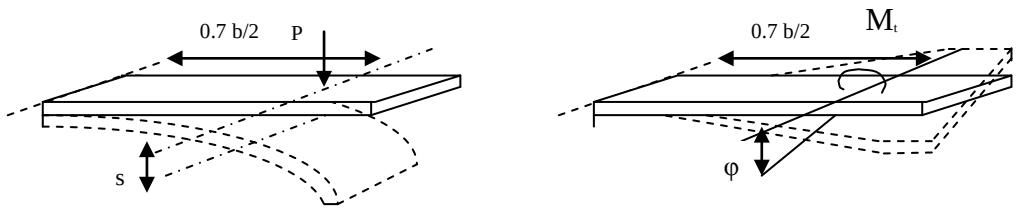

Fig. 6 - Bending and Torsional Stifness Computation.

$$k_B = 0.122\frac{Pb^2}{s} \qquad (2.6) \qquad\qquad k_T = \frac{M_t}{\varphi} \qquad (2.7)$$

The vertical and rotational displacement under these loading conditions, s and φ respectively, can be determined by FEM static analysis in ANSYS®. Consequently, flexural and torsional rigidity (k_B and k_T) values are obtained. It should be noted that this formula considers the half-span the distance from the built-in end to the free end, for which in our case half span is actually the total length of the plate.

2.3 ZAERO® Formulation

The ZAERO® module used for flutter analysis was ZONA6 Unsteady Subsonic Aerodynamics Code which is presented in the Zona ZAERO® Theoretical Manual [28].

2.3.1 ZONA6 Linear Formulation

The ZONA6 code solves the unsteady three-dimensional linearized small-disturbance potential equation of subsonic aerodynamics

$$\left(1-M_\infty^2\right)\Phi_{xx}+\Phi_{yy}+\Phi_{zz}-2\frac{M_\infty}{a_\infty}\Phi_{xt}-\frac{1}{a_\infty^2}\Phi_{tt}=0 \tag{2.8}$$

By assuming a solution of the form

$$\Phi=\phi_0+\phi_1 \tag{2.9}$$

$$\phi_1=\phi e^{i\omega t} \tag{2.10}$$

where

$\phi_1 \ll \phi_0$

M_∞ – freestream Mach number

Φ – total velocity potential

ϕ_0 – steady potential

ϕ_1 – unsteady potential

ϕ – reduced frequency domain potential

ω – oscillation frequency

The steady and unsteady components of equation (2.8) are separated by substituting equations (2.9) into (2.10) and collecting like terms to yield

$$\left(1-M_\infty^2\right)\phi_{0xx}+\phi_{0yy}+\phi_{0zz}=0 \tag{2.11}$$

$$\left(1-M_\infty^2\right)+\phi_{1xx}+\phi_{1yy}+\phi_{1zz}-\frac{2M_\infty}{a_\infty}\phi_{1xt}-\frac{1}{a_\infty^2}\phi_{1zt}=0 \tag{2.12}$$

where equation (2.11) is the steady linearized small disturbance equation and equation (2.12) is the unsteady linearized small disturbance equation. Equation (2.12) is solved after importing the structural mode shapes from ANSYS® model. A set of unsteady pressure coefficients, C_p, is generated using the steady mean flow conditions, unsteady perturbation quantities, reduced frequency, and the mode shapes and their derivatives. These unsteady C_p´s are the basis for the aerodynamic influence coefficient (AIC) matrix relating structural deformations to aerodynamic forces.

2.3.2 Aerodynamic Influence Coefficient Matrix Formulation

In order to generate the flutter solution, a modal *AIC* relating structural mode shapes to unsteady aerodynamic forces must be calculated. By multiplying the area of each box of the plate by the unsteady pressure on that box, the normal force may be computed. After expanding the normal force vector to include the force and moment components, a square matrix relating the structural mode shapes to the aerodynamic forces is constructed as

$$\{L_h\} = q_\infty [AIC]\{h\} \tag{2.13}$$

where

$$[AIC] = [\bar{B}][NIC]^{-1}[\bar{F}] + [\bar{D}] \tag{2.14}$$

$$\{h\} = [T]\{x\} \tag{2.15}$$

$$\{L_h\} = [T][\Phi]\{F_a\} \tag{2.16}$$

where,

q_∞ is the freestream dynamic pressure

$[NIC]$ is the normal velocity influence coefficient matrix

$\{h\}$ is the structural deformation of each aerodynamic box

$\{L_h\}$ is the resultant aerodynamic force vector at each aerodynamic box due to *h*

$[T]$ is the spline matrix relating aerodynamic degrees of freedom to structural degrees of freedom

$[\Phi]$ is the modal transformation matrix

and $[\bar{B}]$, $[\bar{F}]$ and $[\bar{D}]$ are all complex matrices containing the steady mean flow conditions and normal vector components, and are functions of the reduced frequency. Equation (2-14) is defined for the degrees of freedom at the aerodynamic grid points and must be interpolated to the structural grid points using a spline matrix, then transformed to modal coordinates before it is included in the g-method eigenvalue equation.

2.3.3 Flutter Solution Methods

Two basic methods are used to calculate the flutter boundary from the aeroelastic equations of motion: the *k* and *g*-methods. Each method applies the assumption that, at the flutter boundary, one of the natural vibration modes of the system will become neutrally stable and produce simple harmonic motion and the other modes remain stable. The general system of equations for flutter in the Laplace domain may be written as

$$\left[s^2 M + sC + K\right] q = F_a \tag{2.17}$$

where

$M = \Phi^T m \Phi$ is the generalized mass matrix

$K = \Phi^T k \Phi$ is the generalized stiffness matrix

$C = \Phi^T c \Phi$ is the generalized viscous damping matrix

q are the generalized coordinates

F_a are the aerodynamic forces produced by structural deformation

Transforming equation (3.15) into time domain, the basic form of the flutter equation may be written as:

$$\left[-\omega^2 M + K - q_\infty Q(ik)\right] q = 0 \tag{2.18}$$

This equation is solved in ZAERO® using the *k* and *g*-methods. Ref [29] provides a good explanation on both of these methods.

2.3.3.1 K-method

The *k*-method only requires a straightforward complex eigenvalues analysis to be done for all values of reduced frequency *k*. This method assumes the artificial damping first. Flutter speed is located at the point where the value of damping becomes positive. The determinant is obtained by expanding the equation of motion for the flutter system and simplifying the equation by assuming $\lambda = \frac{1+ig}{\omega^2}$. Because of the straightforward eigenvalue analysis, this method has the advantage of computational efficiency. The eigenvalues for the characteristic equation of motion in equilibrium represent a point on the flutter boundary if the corresponding value of *g* equals the assumed value of *g*. The general solution for the characteristic equation is given by the 2nd order polynomial. By solving the polynomial, the roots will yield result in the form of complex numbers. The two complex roots will represent the two modes, which are bending and torsion modes of the plate structure. From there, the values of frequencies, ω, and damping, *g*, can be computed. These series of values of the frequency and the structural damping are obtained for all values of reduced frequency $k = \frac{\omega c}{2V}$. The frequency and damping are then plotted against the airspeed. These curves are known as V-g and V-ω curves. The significance of V-g curve is that the critical flutter speed is achieved when the value of damping is zero, $g = 0$.

2.3.3.2 G-Method

The *g*-method is a method where the first order damping is derived from Laplace domain unsteady aerodynamic forces. The flutter boundary is provided when the value of damping is equal to zero. The solution for this method begins by substituting $p = g + ik$ into the governing

equation. This will result in a second order linear system equation in terms of damping. The solution only exists when the imaginary value of damping is equal to zero. This condition can be acquired by rewriting the 2nd order equation into the form of state space. Then, a technique of reduced frequency sweeps is introduced. This technique seeks the condition where the damping is zero by solving the eigenvalues. The sweeping starts from zero reduced frequency of the unsteady aerodynamic forces with an increment value defined by the user and stops at its maximum value. The frequency and damping is then obtained. Then the V-f and V-g curves can be plotted. As in the *k*-method, the flutter condition occurs where the value of *g* equals zero on the x-axis.

Although the two methods discussed above use different approaches to obtain the plotted values of V-g and V-f curves, they share the same goal which is to locate the point where the damping value equals zero. The *k*-method uses artificial damping to indicate the required damping for the harmonic motion. The damping values do not represent any physical meaning except when the damping value lies at the flutter boundary. In terms of computation time, the solution for the *k*-method is efficient, robust and provides a quicker solution than the *g*-method. In contrast, the discontinuity in damping curves does not occur in the *g*-method because the eigenvalue tracking is done by applying the Predictor-Corrector Scheme. If the eigenvalue changes sharply and creates discontinuity, the scheme will be activated to compute the damping value by reducing the size of the increment of the reduced frequency by a factor.

2.4 Piezoelectric Ceramics

Properties of a poled piezoelectric ceramic element can be explained by the series of images in Fig.7. Mechanical compression or tension on the element changes the dipole moment associated with that element. This creates a voltage. Compression along the direction of polarization, or tension perpendicular to the direction of polarization, generates voltage of the same polarity as the poling voltage. Tension along the direction of polarization, or compression perpendicular to that direction, generates a voltage with polarity opposite to that of the poling voltage. When operating in this mode, the device is being used as a sensor. That is, the ceramic element converts the mechanical energy of compression or tension into electrical energy. Values for compressive stress and the voltage generated by applying stress to a piezoelectric ceramic element are linearly proportional, up to a specific stress, which depends on the material properties. The same is true for applied voltage and generated strain [30].

If a voltage of the same polarity as the poling voltage is applied to a ceramic element, in the direction of the poling voltage, the element will lengthen and its thickness will become smaller. If a voltage of polarity opposite to that of the poling voltage is applied, the element will become shorter and thicker. If an alternating voltage is applied to the ceramic, the element will expand and contract cyclically, at the frequency of the applied voltage. When operating in this mode, the piezoelectric ceramic is used as an actuator. That is, electrical energy is converted into mechanical energy.

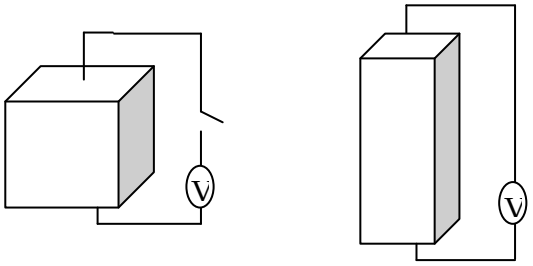

Fig. 7 - Piezoelectric Effect.

2.4.1 Piezoelectric Constitutive Relations

The constitutive equations describing the piezoelectric property are based on the assumption that the total strain in the transducer is the sum of mechanical strain induced by the mechanical stress and the controllable actuation strain induced by the mechanical strain caused by the applied electrical voltage. The axes are identified by numerals rather than letters. The IEEE standard for piezoelectricity [31] suggests that, as in Fig. 8, 1 refers to the x-axis, 2 corresponds to the y-axis, and 3 corresponds to the z-axis. In our case, axis 3 is assigned to the direction of the polarization of the piezoceramic.

The electromechanical equations for a linear piezoelectric material can be written as:

$$\varepsilon_i = S_{ij}^E \sigma_j + d_{mi} E_m \tag{2.19}$$

$$D_m = d_{mi} \sigma_i + \xi_{ik}^\sigma E_k \tag{2.20}$$

where the indexes $i, j = 1, 2, ..., 6$ and $m, k = 1, 2, 3$ refer to different directions within the material coordinate system.

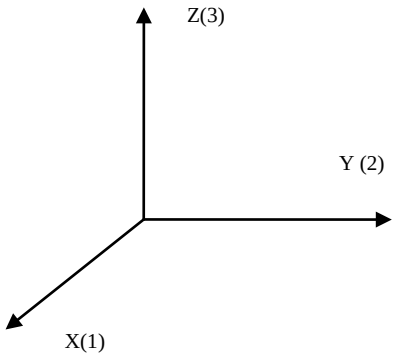

#	Axis
1	x
2	y
3	z
4	Shear around x
5	Shear around y
6	Shear around z

Fig. 8 - Piezoceramic axis convention.

where,

σ is the stress vector (N / m^2)

ε is the strain vector (m / m)

E is the vector of applied electric field (V / m)

ξ is permittivity (F / m)

d is the matrix of piezoelectric strain constants (m / V)

S is the matrix of compliance coefficients (m^2 / N)

g is the matrix of piezoelectric constants (m^2 / C)

The superscripts D, E and σ represent measurements taken at constant electric displacement, constant electric field and constant stress respectively. For a PZT ceramic these parameters can be considered to be:

$$S_{11} = S_{22}$$
$$S_{13} = S_{31} = S_{23} = S_{32}$$
$$S_{12} = S_{21}$$
$$S_{44} = S_{55}$$
$$S_{66} = 2\left(S_{11} - S_{12}\right)$$

$$d_{31} = d_{32}$$
$$d_{15} = d_{24}$$

Piezoelectric actuators are available in different shapes such as rod, plate, etc. The rod type actuators, polarized in the longitudinal direction, are used as stacked actuators in point actuation. The plate type actuators polarized in the thickness direction are used in distributed actuation on plate and shell-like structures. They have electrodes on both sides. The electric field vector $\{E\}$ is the negative gradient of the applied electric potential *V*, the voltage applied in the thickness direction [32], i.e.,

$$\{E\} = -\nabla V \tag{2.21}$$

where

$$\{E\} = \{0, 0, E_z\}^T \tag{2.22}$$

and

$$E_z = -V / t_p \tag{2.23}$$

where t_p is the thickness of the piezoelectric plate. The actuator equation is derived from the constitutive equations with no applied stress in the piezoelectric plate. From the constitutive equations, stresses due to the applied electric field, $\{\sigma_p\}$, in the piezoelectric plate is

$$\sigma_p = \left[\bar{e}\right]^T \{E\} \tag{2.24}$$

where $\{\sigma_p\}$ can be related do the strain in the piezoelectric plate $\{\varepsilon_p\}$ as

$$\{\sigma_p\} = \left|\overline{Q}\right|\{\varepsilon_p\} \tag{2.25}$$

Therefore the strain can be related to the electric field using the above two relations as

$$\{\varepsilon_p\} = \left|\overline{Q}\right|^{-1}\left[\bar{e}\right]^T \{E\} \tag{2.26}$$

By using the above equation and the general strain definition, the total strain vector $\{\varepsilon\}_{tot}$ for electro-elasticity can be written as

$$\{\varepsilon\}_{tot} = \begin{Bmatrix} \{\varepsilon\} \\ \{\varepsilon_p\} \end{Bmatrix} = \begin{Bmatrix} \{\varepsilon\}^l + \{\varepsilon\}^{nl} \\ \{\varepsilon_p\} \end{Bmatrix} \tag{2.27}$$

where $\{\varepsilon\}$ is the elastic strain. This expression for strain is used in the general nonlinear constitutive model of the smart structures with actuators. The electrical displacement in the thickness direction can be written as

$$D_z = e_{31}\{\varepsilon\} \tag{2.28}$$

where e_{31} is the dominant piezoelectric constant. The total charge developed $q(t)$ on the sensor surface is the spatial summation of all point charges and can be calculated by integrating the electric displacement over the sensor surface as

$$q(t) = \int_S D_z dS \tag{2.29}$$

where S is the surface area of the sensor. The open circuit sensor voltage output from the sensors can be written as:

$$\phi_s(t) = G_c i(t) \tag{2.30}$$

where G_c is the gain of the current amplifier. The current $i(t)$ on the sensor is the time derivative of the total charge and can be written as

$$i(t) = \frac{dq(t)}{dt} \tag{2.31}$$

where $q(t)$ is the total charge given by equation 2.29.

2.5 Vibration Suppression Analysis using ANSYS®

It is possible to model active vibration control of a smart a smart plate in ANSYS®. Transient analysis in ANSYS® is carried out for any application to study the system properties with respect to time. Transient vibration analysis gives useful information about system damping and other effects of the controlling forces on vibration with a function of time. Rayleigh damping coefficients should be defined for the closed loop control in this type of analysis. The

logarithmic decrement method was used to compute our structure´s damping ratio where δ is the natural logarithm of the ratio of any two successive amplitudes (x_1 and x_2) and has the following form [33]:

$$\delta = \ln \frac{x_1}{x_2} \tag{2.32}$$

$$\alpha = \frac{\omega_1}{\omega_2} \tag{2.33}$$

$$\beta = \frac{(1-\alpha)\varsigma}{\omega_2 - \alpha\omega_1} \tag{2.34}$$

The damping coefficient value was experimentally determined so that Rayleigh damping coefficients (α and β) could be introduced in the transient analysis. A macro was created in order to apply a voltage to the piezoelectric patches at each different time step so that these exerted a counter force at the plate tip. The scope is to evaluate the decrease of the oscillations amplitude and find an equivalent plate stiffness to introduce in ZAERO®. To do so, different voltage phases were applied according to the displacement of the plate as a function of time.

Chapter 3 – Passive Flutter Solution

The objective of this chapter is to compare three distinct plates in terms of flutter behavior. The first case studied is a 500 mm x 150 mm sandwich plate with a 1 mm thick cork core and one 0.2 mm layer of woven carbon/epoxy at each of the sides. The finite element method and ZAERO® were used to study the dynamic and aeroelastic behavior of this structure. An analytical method was used to calculate the flutter speed and validate the ZAERO® results. These results were further compared to 6061-T6 aluminum and carbon/epoxy plates with 0.75 mm and 1.4 mm thick, respectively. These thicknesses were chosen so that the flight envelope of the three structures would be the same so that attention could be directed to the weight of the components.

3.1 Element Selection

Aluminum, carbon and cork sandwich plate models were built individually in ANSYS® using SHELL63, SHELL99 and SHELL91 elements, respectively. These elements have six degrees of freedom at each node: translations in the nodal x, y and z directions and rotations about the nodal x, y, and z-axes [34]. These modal displacements have to be known to be input in the "free format" ZAERO® modal data file. In the free format it is assumed that the free vibration solution of the finite element model is obtained by a structural finite element code other than NASTRAN. In this case, it is the user's responsibility to set up the modal data in a file according to the following data format:

$$ID, T_1, T_2, T_3, R_1, R_2, R_3$$

where *ID* is the structural grid point (node) identification number, T_1, T_2 and T_3 are the translational modal displacements in x, y, and z directions, and R_1, R_2, and R_3 are the rotational modal displacements about the x, y and z directions. It is also necessary to include the natural frequency and the generalized mass of the modes in the free format file. A modal data file example for the aluminum plate is shown in Fig. 9.

SHELL99 elements were used to model the carbon fiber composite. This element may be used for layered applications of a structural shell like our carbon/epoxy plate. Each

layer thickness is defined as a real constant and it is also possible to set the fiber orientation. SHELL99 element geometry is illustrated in Fig. 10. On the other hand, SHELL91 elements were used to model the cork sandwich since these are more efficient than SHELL99 when building a model using an element with fewer than three layers. Also it has a sandwich structure modeling option, which considers a thick middle layer when compared to the facesheets, although that fact will not take a predominant role in our case since our core is a thin layer of cork agglomerate. The influence of the SHELL91 sandwich option in the plate deformation is presented in Fig. 11.

```
$(Mode 1)
8.24866     0.1E+01     $Circular Frequency and Generalized Mass
     $(ID)   T1           T2           T3          R1          R2          R3
       1   0.0000      0.0000       0.0000      0.0000      0.0000      0.0000
       2   0.0000      0.0000       0.0000      0.0000      0.0000      0.0000
       3   0.0000      0.0000       0.0000      0.0000      0.0000      0.0000
       4   0.0000      0.0000       0.0000      0.0000      0.0000      0.0000
       5   0.0000      0.0000       0.0000      0.0000      0.0000      0.0000
       6   0.0000      0.0000       0.0000      0.0000      0.0000      0.0000
       7   0.0000      0.0000       0.0000      0.0000      0.0000      0.0000
       8  -0.56132E-15 0.28026E-15  6.9299      19.337      0.10231     0.25815E-14
       9   0.99320E-17 0.13921E-16  0.91902E-01 3.9392      1.0063     -0.32719E-15
      10   0.15721E-16 0.41800E-16  0.39601     8.0992      1.3593      0.10387E-15
      11   0.12079E-16 0.75084E-16  0.88888     11.515      1.3074      0.13962E-15
      12  -0.97657E-17 0.11842E-15  1.5342      14.216      1.1082      0.76393E-15
      13  -0.56698E-16 0.16712E-15  2.2978      16.259      0.86447     0.10924E-14
      14  -0.13860E-15 0.21204E-15  3.1484      17.703      0.62387     0.20778E-14
      15  -0.23321E-15 0.24417E-15  4.0579      18.625      0.41263     0.17581E-14
      16  -0.33696E-15 0.26574E-15  5.0025      19.119      0.24827     0.23482E-14
      17  -0.44512E-15 0.27589E-15  5.9638      19.304      0.14408     0.20089E-14
(...)
$(Mode 2)
51.79669     0.1E+01
       1   0.0000      0.0000       0.0000      0.0000      0.0000      0.0000
       2   0.0000      0.0000       0.0000      0.0000      0.0000      0.0000
       3   0.0000      0.0000       0.0000      0.0000      0.0000      0.0000
       4   0.0000      0.0000       0.0000      0.0000      0.0000      0.0000
       5   0.0000      0.0000       0.0000      0.0000      0.0000      0.0000
       6   0.0000      0.0000       0.0000      0.0000      0.0000      0.0000
       7   0.0000      0.0000       0.0000      0.0000      0.0000      0.0000
       8  0.11857E-16 -0.18360E-17  6.8802      67.999      2.4293     -0.21886E-16
       9  0.35270E-18 -0.51023E-18 -0.58298    -22.597     -2.5931     -0.14631E-16
      10  0.10975E-17 -0.95880E-18 -2.0368     -33.557     -0.17751    -0.11952E-16
      11  0.19405E-17 -0.12565E-17 -3.6722     -30.310      3.6327     -0.24166E-16
      12  0.30897E-17 -0.14306E-17 -4.8554     -15.973      6.8481     -0.19168E-16
      13  0.41380E-17 -0.17226E-17 -5.1402       5.0456     8.5887     -0.29868E-16
      14  0.53918E-17 -0.17964E-17 -4.3179      27.723      8.6224     -0.24651E-16
      15  0.70817E-17 -0.16908E-17 -2.4254      47.367      7.2362     -0.30795E-16
      16  0.86491E-17 -0.17502E-17  0.29791     60.689      5.1367     -0.23860E-16
```

Fig. 9 - Zaero Modal Data Input File.

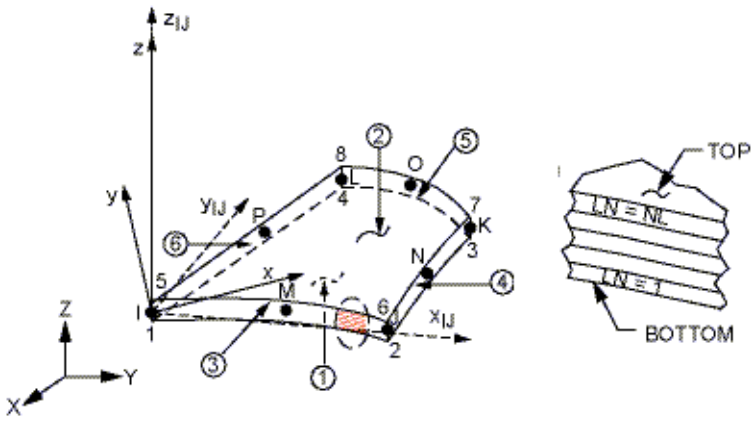

Fig. 10 - SHELL99 Element Geometry.

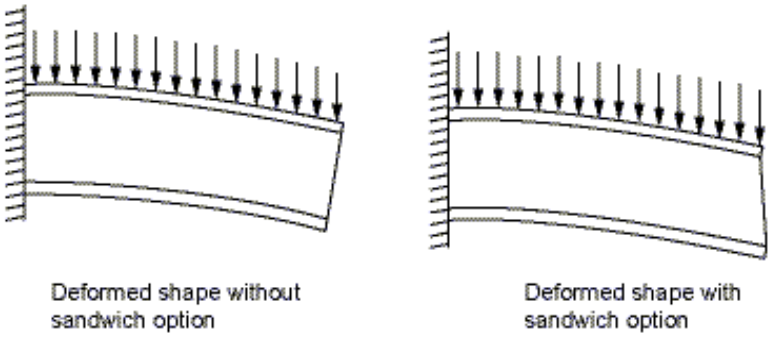

Fig. 11 - SHELL91 Sandwich Option.

3.2 Mesh Sizing

In order to validate the chosen elements and mesh size, simple Euler-Bernoulli Beam Theory was used to compute tip deflection of a cantilever plate loaded at the free end and the theoretical results were compared with finite element results. The material and geometric properties assigned for each case are presented in Table 1. The thickness of the sandwich was chosen in order to ensure manufacture feasibility with 2 carbon/epoxy facesheets (0.2 mm each) and a 1 mm thick cork core. The other plates thicknesses were chosen in order obtain the same flight envelope (same flutter onset speed) as the cork sandwich.

Table 1 - Material and geometrical properties.

Material Properties			
	Aluminum	Carbon/Epoxy	Cork
E_x, GPa	68.9	42	0.032
E_y, GPa	-	42	0.032
G_{xy}, GPa	-	5	0.005
υ	0.33	0.1	0.26
ρ, kg/m^3	2800	1400	300
Geometrical Properties			
b, m	0.5	0.5	0.5
c, m	0.15	0.15	0.15
t, m	0.00075	0.00140	0.00140

The plate deflection results are presented in Table 2.

Table 2 - Tip deflection results for mesh definition.

Mesh 10 x 6	Aluminum	Carbon/Epoxy	Sandwich
P, N	1	1	1
$Y_{Theoretical}$, m	0.11470	0.02892	0.04549
Y_{FEM}, m	0.11590	0.02889	0.04548
Error, %	1%	0.11%	0.02%

The 10 x 6 element mesh size guarantees a good agreement between theoretical and finite element analysis.

3.3 Flutter Speed Determination using the Semi-Analytical Method

For the analytical flutter speed computation, a unit load and moment at 70% of half span and at half chord was applied to the sandwich plate. The finite element solution provides the translational and rotational displacements for the bending and torsional rigidities computation. Table 3 presents the flutter speed result using this method.

Table 3 - Flutter speed determination by semi-analytical method.

Sandwich Parameters	
r_e, m	0.075
r_m, m	0.075
Λ	6.667
k_T, N/rad	0.0143
k_B, N/m	0.0783
c_m, m	0.15
F, m^2	0.15
m, kg	0.129
ρ_{air}, kg/m^3	1.225
M_t, N.m	0.01
φ, rad	0.7006
P, N	0.01
s, m	0.0156
V_f, m/s	19.86
V_f / *Mass*	153.95

As we can see, the determination of flutter speed depends on several parameters like plate geometry, aspect ratio, density ratio, and particularly on bending and torsional rigidities. Although the sandwich plate has a lower torsional rigidity, it has a much greater bending rigidity than those of aluminum and carbon due to a higher second moment of area. As the first mode of vibration of a cantilever plate is usually a pure bending mode, shifting the occurrence of this

mode of vibration to a higher natural frequency will prevent the occurrence of flutter. In the next sections, these results will be compared to conventional carbon/epoxy and aluminum plates.

3.4 ANSYS® Modal Analysis

The first ten modes of vibration and frequencies were extracted using ANSYS® modal analysis.

In Fig. 12, the sandwich mode shapes extracted from ANSYS® modal analysis are represented. For each of these structural eigenvectors there is a corresponding eigenvalue. The response of the plate amplifies as we apply a force with a rate of oscillation that gets closer and closer to the natural frequency of the system and reaches a maximum when the rate of oscillation is at the resonant frequency.

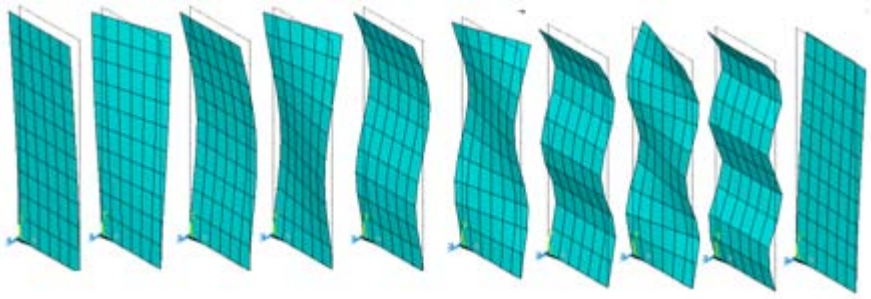

Fig. 12 - Sandwich Mode Shapes.

3.5 ZAERO® Output Results

After running ZAERO® aeroelastic code (Annex A) based on ANSYS® modal analysis, several files are generated. Fig. 14 shows the aerodynamic grid model generated by ZAERO®. Each division represented is called a wing box. To construct an *AIC* matrix for the wing like component it is necessary to compute the aerodynamic force acting normal to the wing boxes. This force can be obtained by multiplying the area of the wing boxes to the unsteady pressure on wing boxes. This ZAERO® demo version is limited to 40 wing boxes, although it is expected that this fact will not affect greatly the results obtained. The semi-analytical method was used to ensure that ZAERO® results were reliable.

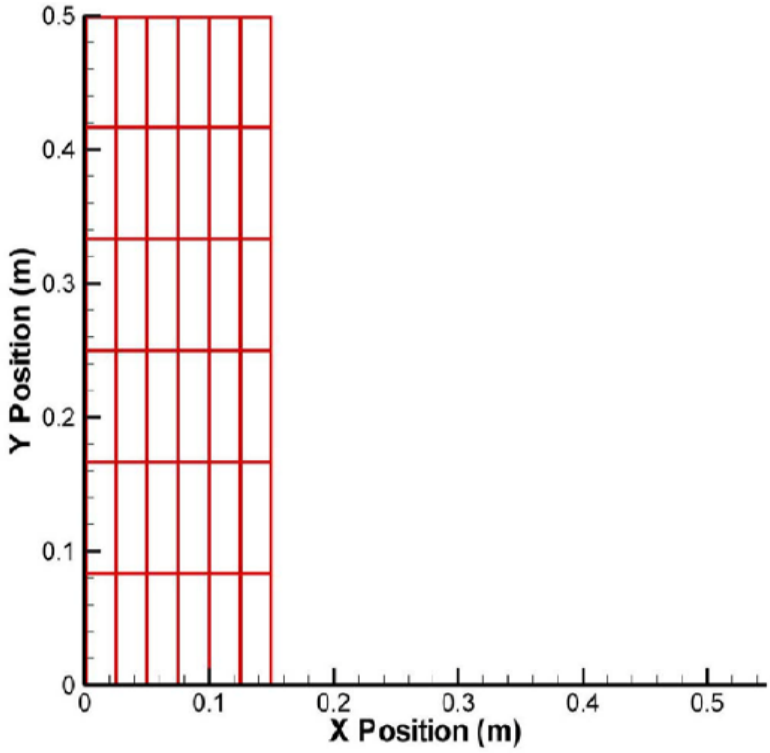

Fig. 13 - Aerodynamic Grid.

FLUTTER AT MODE NO.: 2	G= 0.00%	G= 0.50%	G= 1.00%	G= 1.50%	G= 2.00%	G= 2.50%	G= 3.00%	G= 3.50%	G= 4.00%
SPEED |UNITS= M / SEC	19.9076	19.9846	20.0603	20.1358	20.2110	20.2849	20.3588	20.4310	20.5012
V/VREF|UNITS= NONE	19.9076	19.9846	20.0603	20.1358	20.2110	20.2849	20.3588	20.4310	20.5012
FREQ |UNITS= HZ	15.8316	15.7872	15.7440	15.7011	15.6584	15.6174	15.5763	15.5381	15.5035
DYN P |UNITS=KG /M /S**2|	2.427+02	2.446+02	2.464+02	2.483+02	2.501+02	2.520+02	2.538+02	2.556+02	2.574+02

DYNAMIC PRESSURE AT G=0.0, W = 15.8316 HZ, V = 1.9908E+01 :
COMPUTED = 2.4268E+02, INTERPOLATED = 2.4274E+02, ERROR = -2.5245E-02%. CORRESPONDING EIGENVECTOR OF 10 MODES =
1.000E+00 0.000E+00, -3.454E-01 3.503E-01, 7.685E-02 -3.682E-02, 2.197E-03 -6.859E-03, -1.568E-05 1.562E-03,
1.649E-04 6.671E-05, 5.021E-04 -2.023E-04, -1.447E-04 1.764E-04, 2.078E-05 7.787E-05, -2.460E-13 -1.702E-12,

FLUTTER MODE TRACKING: 100% = PRIMARY MODE. 0% = NO CONTRIBUTION TO FLUTTER MODE.
MODE(1) = 14.8575%, MODE(2) = 100.0000%, MODE(3) = 0.9000%, MODE(4) = 0.2110%, MODE(5) = 0.0075%,
MODE(6) = 0.0007%, MODE(7) = 0.0030%, MODE(8) = 0.0021%, MODE(9) = 0.0011%, MODE(10) = 0.0000%,

Fig. 14 - ZAERO® g-method Output File.

ZAERO® flutter analysis output file is represented in Fig. 15. It shows the mode at which flutter occurs and the corresponding speed and frequency, 19.91 m/s and 15.83 Hz respectively, as well as the value of the dynamic pressure at which this occurs, in this case, 242.6 N/m^2. The second

structural mode, which corresponds to the first torsion mode, has a predominant role in the occurrence o flutter (100%) while the first bending mode contributes by 14.86%. This means that if the structure did not have the first bending mode, its flutter behavior would change slightly while if it did not have the torsion mode its behavior would change dramatically.

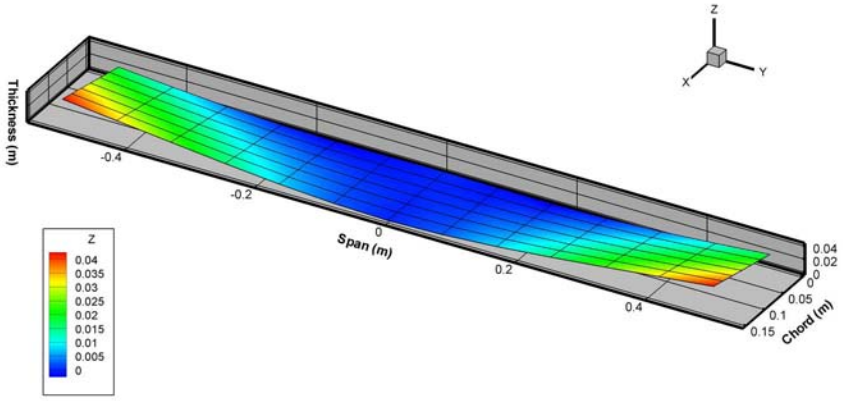

Fig. 15 – Sandwich Flutter Mode – Deformed Aerodynamic Mesh.

In Fig. 16, flutter mode is represented by the deformed aerodynamic model. Since the flutter mode does not have a nodal line about which the configuration oscillates (as in the case of the structural model results), it is necessary to generate many deformed aerodynamic models to notice the dynamics of the flutter mode. Only the maximum displacement of the flutter mode shape is shown in Fig. 16. We can clearly see that the flutter mechanism consists of a coupling between first bending and torsion modes which are represented in Fig. 17 and Fig. 18, respectively. The maximum displacement of the oscillation in the z-direction during the flutter mode is about 0.045 m. As it has been mentioned earlier, this value is computed having in mind that the aerodynamic force that causes the deflection is given by the unsteady *Cp´*s multiplied by each wing box area. By default, ZAERO® plots a full span symmetric wing cantilevered at the middle in flutter mode.

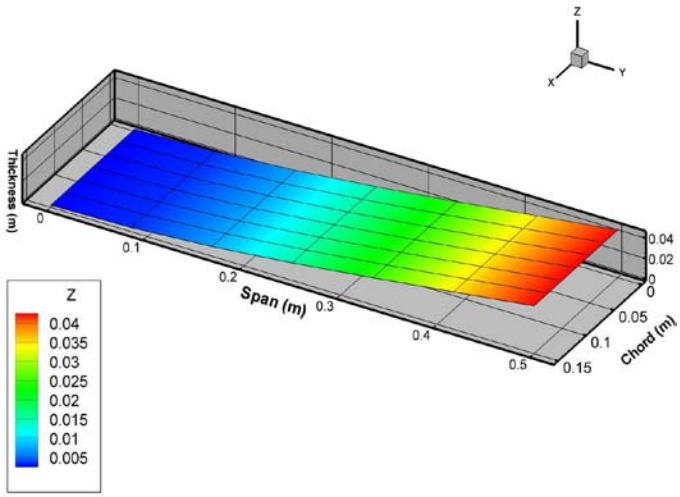

Fig. 16 - Sandwich First Bending Mode – Deformed Aerodynamic Mesh.

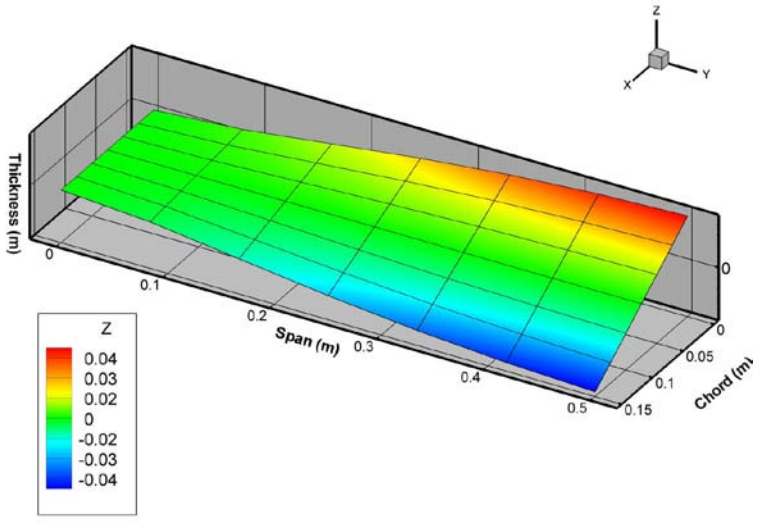

Fig. 17 - Sandwich First Torsion Mode – Deformed Aerodynamic Mesh.

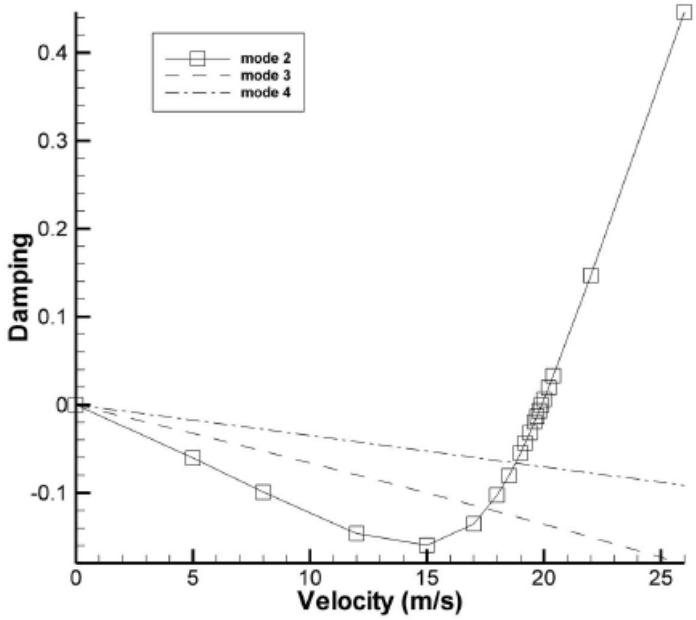

Fig. 18 –Sandwich V-g Diagram.

A tracking procedure is provided by ZAERO® using the most relevant modes of vibration of the composite sandwich. Fig. 19 plots the aerodynamic damping on the vertical axis versus velocity on the horizontal axis and Fig. 20 plots the frequency on the vertical axis also versus velocity on the horizontal axis. Although the horizontal axis for both plots is in meters per second, it is also representative of increasing density with decreasing altitude. This is due to the fact that velocity for a given Mach number is a function of the square root of the air density. In Fig. 19, positive and negative dampings are representative of stable and unstable conditions, respectively. As we can see, flutter occurs when the velocity curve intercepts the zero damping line. This means that at this velocity, if the structure suffers an excitation, the aerodynamic flow will no longer damp the structural vibration. One is then able to determine the flutter frequency of the model using the plot of Fig. 20 and picking off the frequency value of the unstable mode at the flutter velocity value. The slope of the damping versus velocity curve as it passes through flutter velocity can be thought of as a qualitative measure of how violently the oscillations would occur during accelerated flight.

In order to compare the results with the sandwich, thicknesses of the aluminum (0.75 mm) and carbon/epoxy (1.3 mm) plates were chosen in order to have an equal flutter onset speed. Fig. 20 shows a comparison of the V-g diagram for aluminum, carbon/epoxy and cork sandwiches.

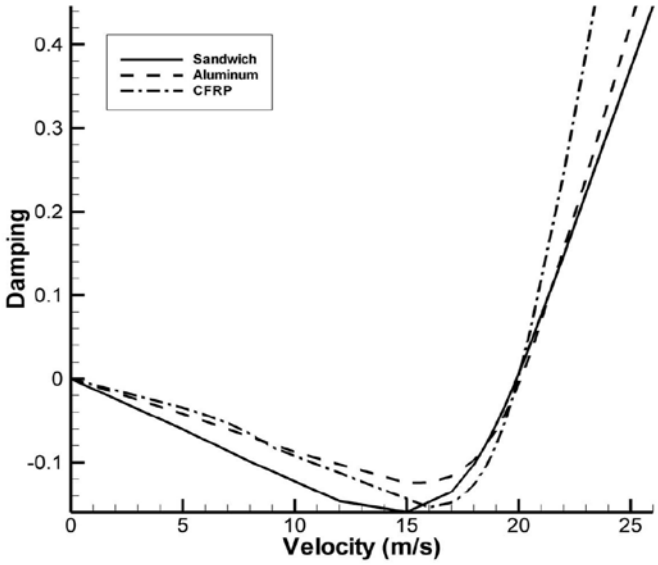

Fig. 19 - Comparison between V-g Diagrams.

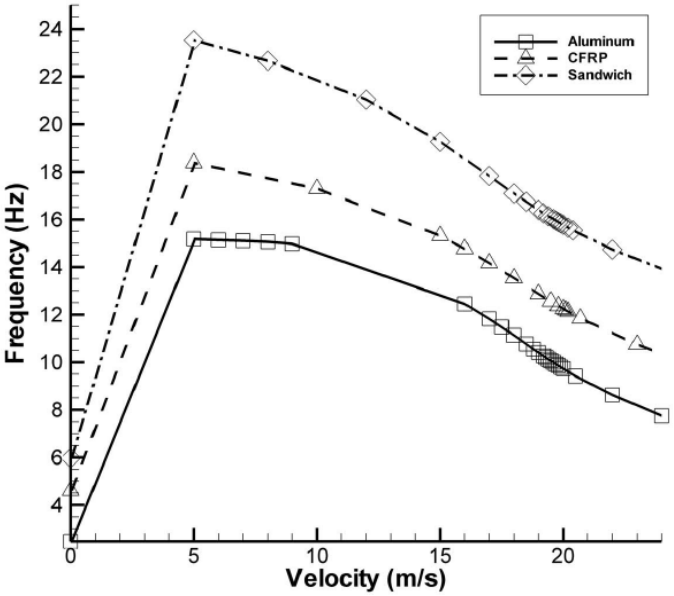

Fig. 20 - Comparison between V-f Diagrams.

Table 4 – V_f/mass results and comparison.

	Aluminum (0.75 mm)	CFRP (1.4 mm)	Sandwich (1.4 mm)
Flutter Speed Analytical, m/s	19.65	20.48	19.87
Flutter Speed g – Method, m/s	19.98	20.87	19.92
Flutter Speed k- Method, m/s	20.00	20.90	19.80
Rigidity, N.m	0.363	1.44	0.916
Specific Rigidity, $N.m^2/\rho$	$1,30\times10^{-4}$	1.03×10^{-3}	$1,49\times10^{-3}$
Mass, kg	0.158	0.116	0.065
V_f / Mass, m/s.kg	125.8	180.17	306.5

Although the three plates are limited by the same flight envelope, the cork sandwich ensures a lighter structure and, therefore, a higher ratio $\frac{V_F}{m}$ as it is shown in Table 4. This is due to the fact that the higher second moment of area provided by the sandwich shifts the natural frequencies of the first bending and torsion modes, the most critical ones, to higher values as represented in Fig. 20 and quantified in Table 5.

Table 5 - Natural frequencies comparison [Hz].

Mode	Aluminum	CFRP	Sandwich
1	2.46	4.61	5.97
2	15.48	18.86	24.36
3	16.54	28.86	37.38
4	43.81	61.99	80.03

It is interesting to notice, however, that even with the same thickness, without the second moment of area taking a predominant role, the sandwich structure ensures practically the same flight envelope than the carbon-epoxy plate, although with a much lower weight.

Chapter 4 – Active Flutter Solution

In this chapter, a preliminary computational study on an active control concept using piezoelectric ceramics is performed. Six BM500 ceramics (20 mm x 28 mm x 0.25 mm) were attached to a host aluminum plate with dimensions 500 mm x 150 mm x 0.4 mm and modeled using ANSYS® piezoelectric analysis. A study based on high strain energy locations of the plate´s most critical modes of vibration was performed in order to choose the piezoelectric patches placement. Using transient analysis, one evaluated the oscillations amplitude of the actuated and not actuated plate with the objective of analyzing how does the actuation of the piezoelectric affects the rigidity of the plate. Using this data, the flutter speed increment due to this active concept was computed.

4.1 Piezoelectric patches placement

Placement of piezoelectric patches was chosen via strain analyses. FEM strain energy plots for the first three modes of vibration were produced and analyzed using ANSYS® to determine the predicted locations of concentrated strain energy for each mode. By determining areas of concentrated strain energy, it was possible to choose the general placement locations for each mode based upon existing FEM elements. The patches were located in such a manner as to cover the regions of higher strain in a combined solution between the first bending mode and the first torsion mode. It is not the scope of this work to study an optimal location for the actuators. Besides the FEM strain analysis, piezoelectric placement was also based on literature review on this matter.

As we have seen in Chapter 3 there are two modes of vibration which contribute the most for the occurrence of flutter. In the case of 0.4 mm thickness aluminum plate, which was studied for the active vibration control, these modes are the first bending (11.55%) and the first torsion mode (100%).

Plots of strain distribution are shown in Fig. 21 and Fig. 22 for the first two modes.

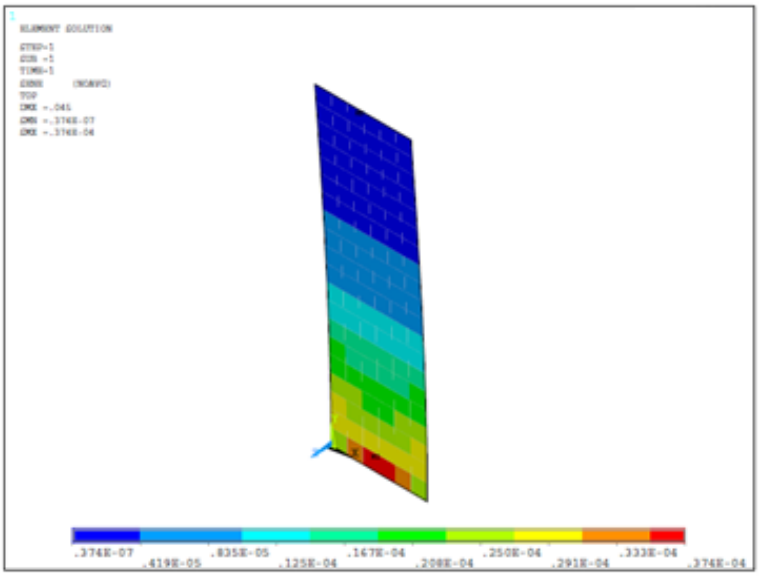

Fig. 21 - Srain Energy Distribution in Bending Mode.

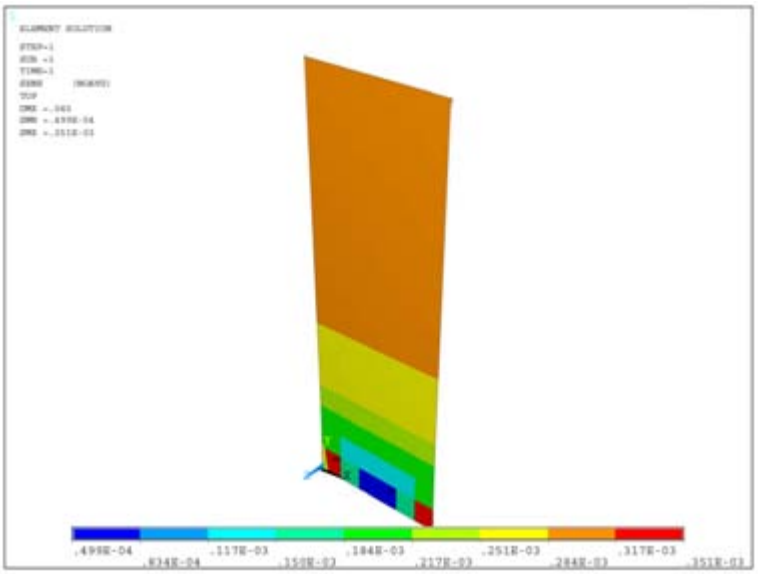

Fig. 22 - Strain Energy Distribution in Torsion Mode.

It is clear that for the bending mode the actuators should be placed near the built-in end while for the torsion mode they should be at the free end. However, it must be noted that in the bending mode there is a significant change of strain energy density between the near built-in end and free end position. In the torsion mode, this change is not so dramatic. This means that placing the actuators near the free end position would substantially affect the efficiency of the actuators at

bending, while placing the actuators near the built-in end will not influence the torsion efficiency that much. For this reason, the following configuration was chosen using 6 BM500 (20 mm x 28 mm x 0.25 mm) actuators.

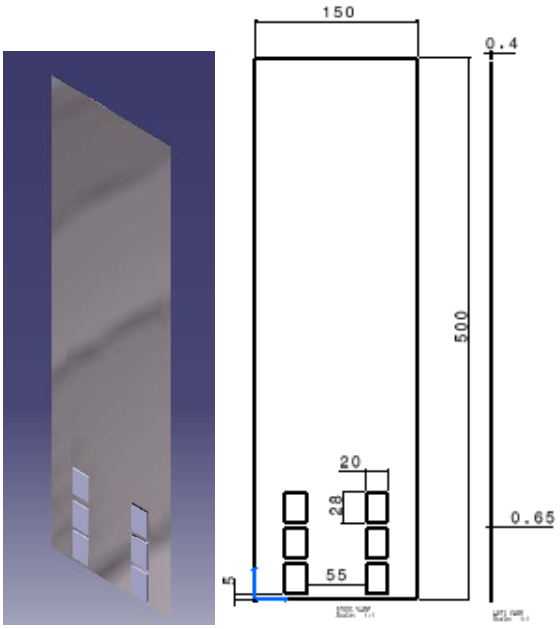

Fig. 23 - Smart Plate Configuration and Dimensions.

4.2 Static Smart Plate Analysis

The purpose of the actuators is to generate bending and torsion moments in the plate. In the case of bending, this is done by applying equal voltage magnitudes and phases to the ceramic patches. In the torsion case, the voltage is applied in a 180º out of phase difference to the left and right side patches of the plate. Due to the phase difference between voltages applied to the actuators, patches from the left side of the torsion axis will expand while the others contract, or vice-versa. This will impart a positive or negative torsion moment to the host structure.

A plate model with dimensions 500 mm x 150 mm x 0.4 mm was built in ANSYS® using SOLID45 elements to model the metal part. This element is defined by eight nodes having three degrees of freedom at each node: translations in the nodal *x*, *y*, and *z* directions. The piezoelectric patches were modeled using SOLID5, a 3D coupled field element. For this piezoelectric element there are four degrees of freedom at each node; translations in the *x*, *y* and *z* directions and *VOLT*. In this case, it is necessary to use coupled field analysis to couple the interaction between applied stress and electric field. The brick shaped element SOLID5 was chosen due to the fact

that the geometrical shape of the piezoelectric actuator does not have any curvature and SOLID5 constructs with cuboid elements. Also, this element is capable of modeling different types of disciplines, namely piezoelectricity. When this particular type of discipline is chosen, ANSYS® will only consider the behavior of SOLID5 in u_x, u_y, u_z and *VOLT* degrees of freedom. *VOLT* indicates the difference in potential energy of the electrical particles between two locations.

Although the constitutive piezoelectric relation given by the manufacturer is the form described in Chapter 2, the constitutive equations that ANSYS® uses to model piezoelectric materials requires data in the following form:

$$\begin{Bmatrix} \{T\} \\ \{D\} \end{Bmatrix} = \begin{bmatrix} [c] & [e] \\ [e^T] & [-\varepsilon] \end{bmatrix} \begin{Bmatrix} \{S\} \\ \{-E\} \end{Bmatrix} \tag{4.1}$$

where,

{T} is the stress vector

$\{D\}$ is the electric flux density vector

$\{S\}$ is the strain vector

$\{E\}$ is the electrical field vector

$[c]$ is the elasticity matrix at constant electric field

$[e]$ is the piezoelectric stress matrix

$[\varepsilon]$ is the dielectric matrix at constant mechanical strain

Therefore, ANSYS® only considers these material properties for piezoelectric 3-D elements, including compliance matrix, piezoelectric matrix, and permittivity matrix given below:

The elasticity matrix:

$$c = \begin{bmatrix} c_{11} & c_{12} & c_{13} & 0 & 0 & 0 \\ c_{12} & c_{22} & c_{23} & 0 & 0 & 0 \\ c_{13} & c_{23} & c_{33} & 0 & 0 & 0 \\ 0 & 0 & 0 & c_{44} & 0 & 0 \\ 0 & 0 & 0 & 0 & c_{55} & 0 \\ 0 & 0 & 0 & 0 & 0 & c_{66} \end{bmatrix} \tag{4.2}$$

The piezoelectric matrix:

$$e = \begin{bmatrix} 0 & 0 & d_{31} \\ 0 & 0 & d_{32} \\ 0 & 0 & d_{33} \\ 0 & d_{24} & 0 \\ d_{15} & 0 & 0 \\ 0 & 0 & 0 \end{bmatrix} \tag{4.3}$$

The dielectric matrix:

$$\varepsilon = \begin{bmatrix} \varepsilon_{11} & 0 & 0 \\ 0 & \varepsilon_{22} & 0 \\ 0 & 0 & \varepsilon_{33} \end{bmatrix} \tag{4.4}$$

In order to convert the manufacturer´s data presented in the form of equations 2.19 and 2.20 to ANSYS® notation, eq. 4.1 needs to be based on stress rather than strain. One can obtain the relationship between the manufacturer´s supplied data and ANSYS® required values through the following transformation:

$$\begin{aligned} \left[c^E\right] &= \left[S^E\right]^{-1} \\ \left[\varepsilon^S\right] &= \left[\varepsilon^T\right] - [d]^t \left[S^E\right]^{-1} [d] \\ [e] &= \left[S^E\right]^{-1} [d] \end{aligned} \tag{4.5}$$

A small code was built in MATLAB® in order to convert the data (Annex B).

The supplied manufacture data provided by the manufacturer and the converted data to ANSYS® is presented in Table 6:

Table 6 - BM500 properties.

BM500 Ceramics			
Manufacturer Data		ANSYS® Input Data	
d_{31}, m/V	$-175e^{-12}$	e_{31}, C/m^2	-7.59
d_{33}	$365e^{-12}$	e_{33}	13.62
d_{15}	$585e^{-12}$	e_{15}	13.0
$S_{11,}$ m^2/N	$15.5e^{-12}$	$c_{11,}$ N/m^2	$118e^{9}$
S_{33}	$19.0e^{-12}$	c_{33}	$103.5e^{9}$
S_{12}	$-5.0e^{-12}$	c_{12}	$69.2e^{9}$
S_{13}	$-7.0e^{-12}$	c_{13}	$70e^{9}$
S_{44}	$4.5e^{-12}$	c_{44}	$24.4e^{9}$
S_{66}	$4.10e^{-12}$	c_{66}	$22.2e^{9}$
$\varepsilon_{11}/\varepsilon_0$, F/m	1650		
$\varepsilon_{33}/\varepsilon_0$	1750		
ρ, kg/m^3	7650		

Cantilever boundary conditions were defined for the smart plate. After meshing, the electrical degrees of freedom of the piezoelectric patch, *VOLT*, are coupled at the outer surfaces of the actuators and the intermediate common surfaces between the actuators and the plate. This simulates a set of electrodes at the outer and intermediate faces and couple the electrical and mechanical disciplines. Applying a voltage to the master node of each coupled set will act as voltage applied to the whole PZT surface. Depending on the phase of the applied voltage, the actuators will extend or contract. Fig. 25 shows the modeled mesh with the coupled sets.

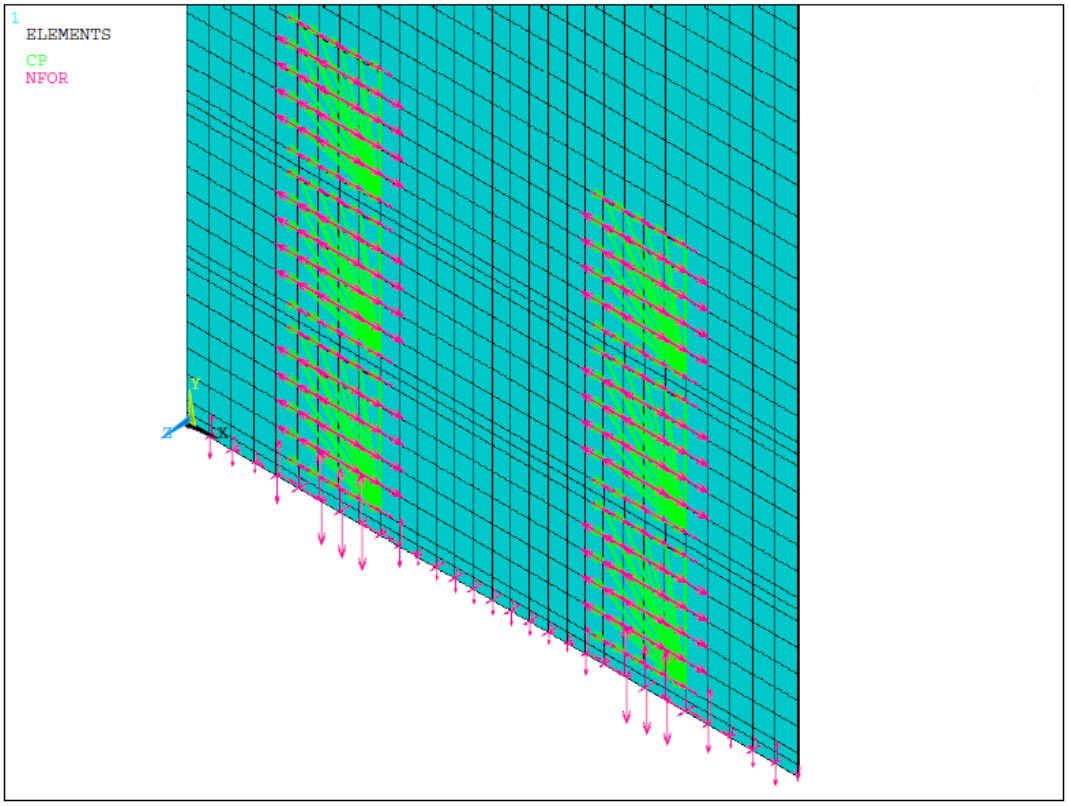

Fig. 24 - Piezoelectric Mesh and Coupling.

Static simulations were performed in ANSYS® in order to analyze the maximum tip displacements of the plate. Bending and torsion deformed shapes are represented in Fig. 26 and Fig. 27, respectively. A range of voltage was applied to each ceramic being the maximum value of 250 V. This is due to the fact that BM500 ceramics have a maximum voltage of about 1000 V/mm. Therefore the actuator voltages must be kept under 250 V. As it was expected, there is a greater efficiency in the bending actuation than in the torsional actuation. This is the reason why controlling the torsion mode using piezoelectric actuators is still a great challenge and not a common practice in full scale aircraft.

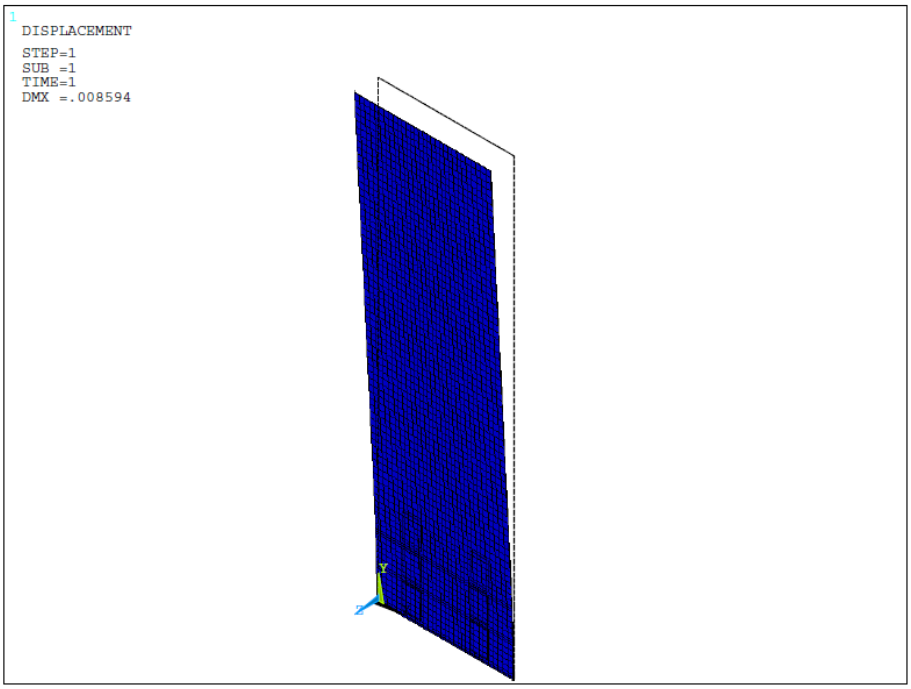

Fig. 25 - Maximum Actuated Bending Deflection.

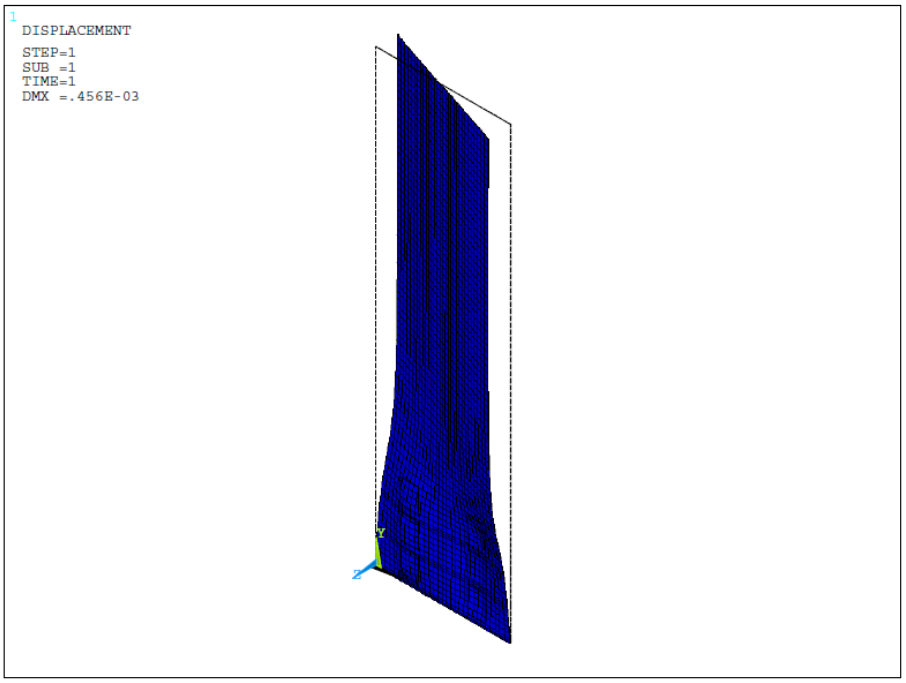

Fig. 26 - Maximum Actuated Torsion Delection.

In Fig. 28 the plate tip displacement is plotted as a function of the applied voltage in the actuators.

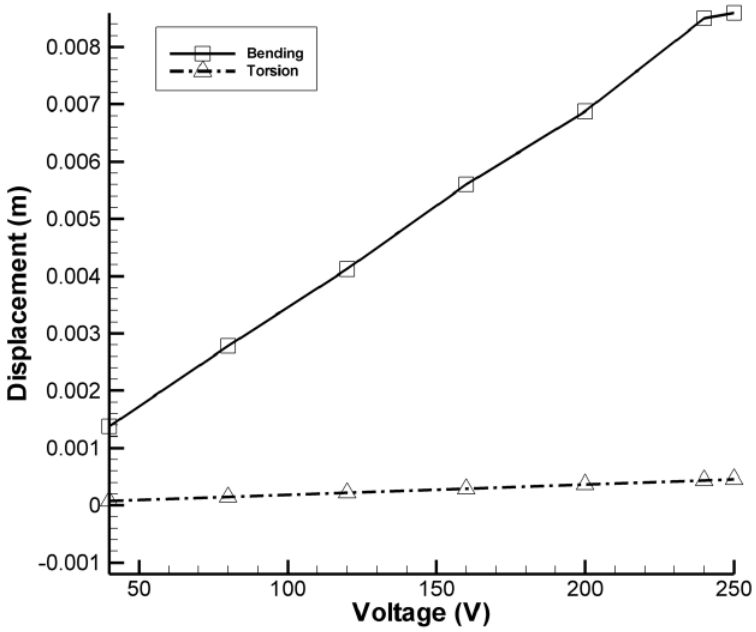

Fig. 27 - Bending and Torsion Voltage-Displacement Diagram.

4.3 Damping Properties of the Aluminum Plate

In the transient dynamic analysis, it is necessary to apply Rayleigh damping. Rayleigh damping is characterized by the two constants α and β and the aluminum plate´s damping coefficient ζ. Using the logarithmic decrement method, ζ was determined experimentally to be 0.0006. Performing ANSYS® modal data, α and β were determined through the following equations:

$$\alpha = \frac{\omega_1}{\omega_2} \qquad \beta = \frac{(1-\alpha)\varsigma}{\omega_2 - \alpha\omega_1} \tag{4.9}$$

where ω_1 and ω_2 are the two lowest frequencies. The values of $\alpha = 0.159$ and $\beta = 9\times10^{-6}$ were used in the transient analysis of which there is a representation in Fig. 28 where the damping behavior of the plate when it suffers an excitation in the form of a tip load below the critical flutter speed is represented.

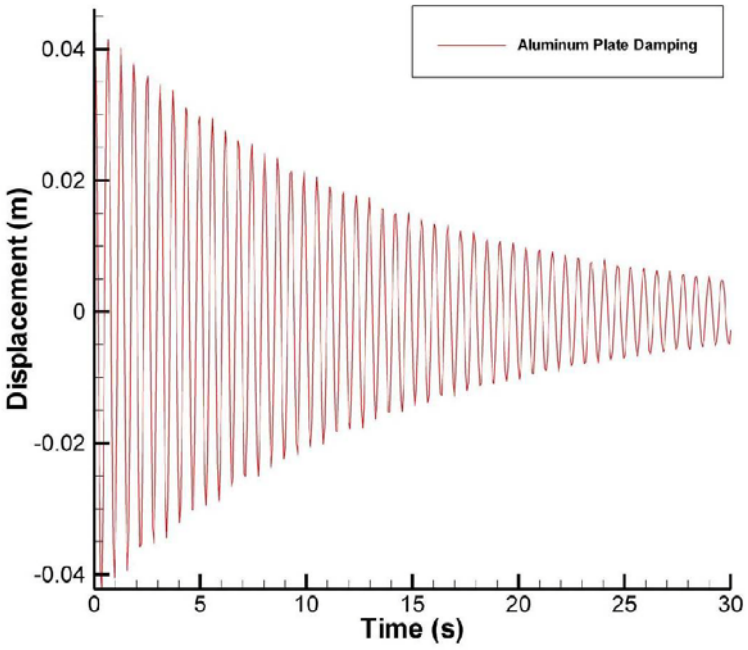

Fig. 28 - Aluminum Plate Structural Damping.

On the other hand, if the excitation occurs above the critical flutter speed, the structure will no longer be damped. Fig. 29 plots the displacement amplitude-time curve for the undamped structure. The maximum displacement is based on ZAERO® output results for the aluminum plate. Actuators will be modeled in order to decrease the amplitude of these oscillations and increase flutter speed.

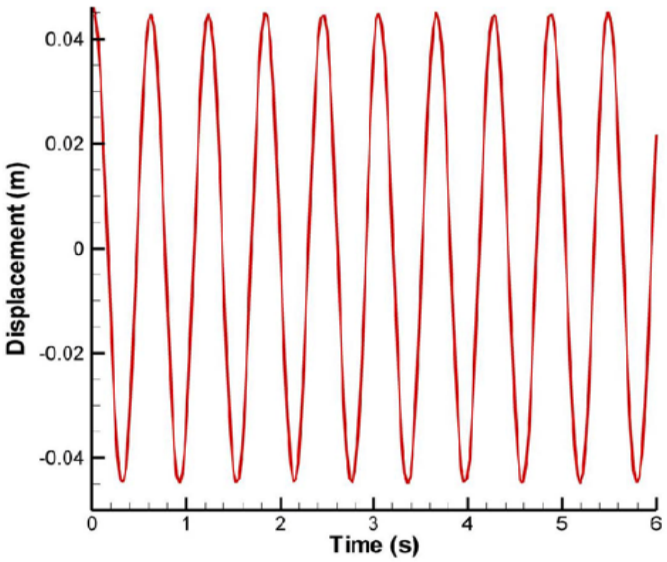

Fig. 29 - Aluminum Plate Structural Damping Above Critical Flutter Speed

4.4 Flutter Speed Increment due to Actuation

When a piezoelectric patch is excited with a voltage it exerts control over the rigidity and damping characteristics of the host structure. The effect on rigidity can be considered using a simple Euler-Bernoulli cantilever beam problem. The rigidity of the plate is a function of the applied force and the displacement due to such force. The higher the displacement is, the smaller the rigidity of the plate. One can also think in terms of damping. Stiffer structures have smaller oscillation amplitudes than less rigid structures. If a voltage is applied to the actuators to counter this displacement, the structure gains rigidity. The effect of a 250 V and a 100 V actuation on the plate rigidity was analyzed. Fig. 30 shows the reduction of the amplitude oscillation due to the actuation of the piezoelectric.

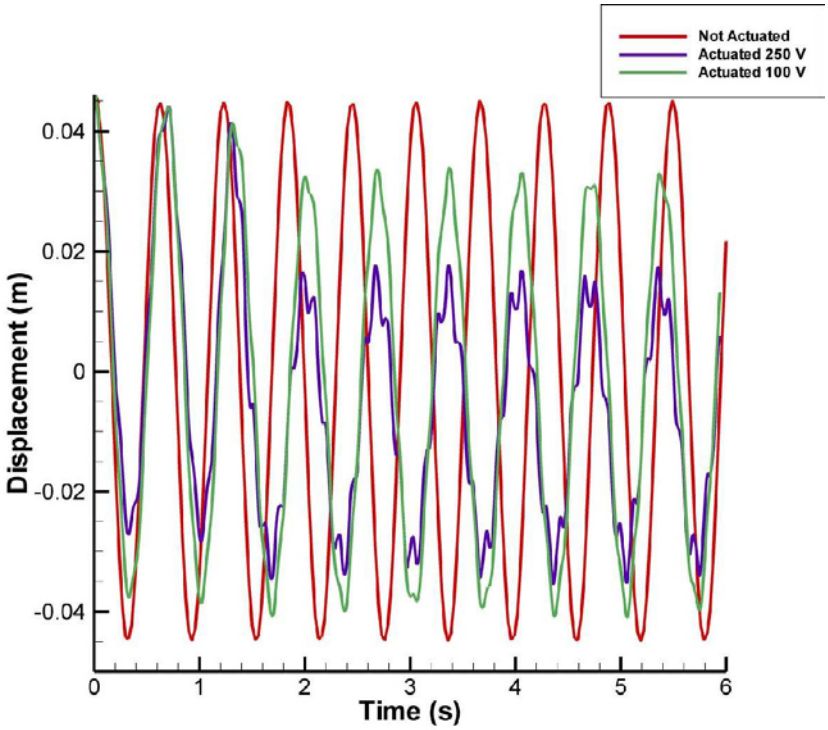

Fig. 30 - Active Oscillation Control.

This data was then exported to ZAERO® in order to compute the flutter speed increment due to actuation considering an equivalent plate with the same rigidity as the actuated with 250 V. Table 7 shows the increment in flutter speed using piezoelectric actuation.

Table 7 - 250 V piezoelectric actuation influence on plate's flutter speed.

	Aluminum 0.4 mm	Aluminum 0.4 mm + 6 PZT
Flutter Frequency (Hz)	5.25	6.56
Flutter Speed G-Method (m/s)	8.16	10.26
Flutter Speed K-Method (m/s)	8.20	10.30
Mass (kg)	0.0840	0.0851
V_f / Mass (m/s.kg)	97	120.6

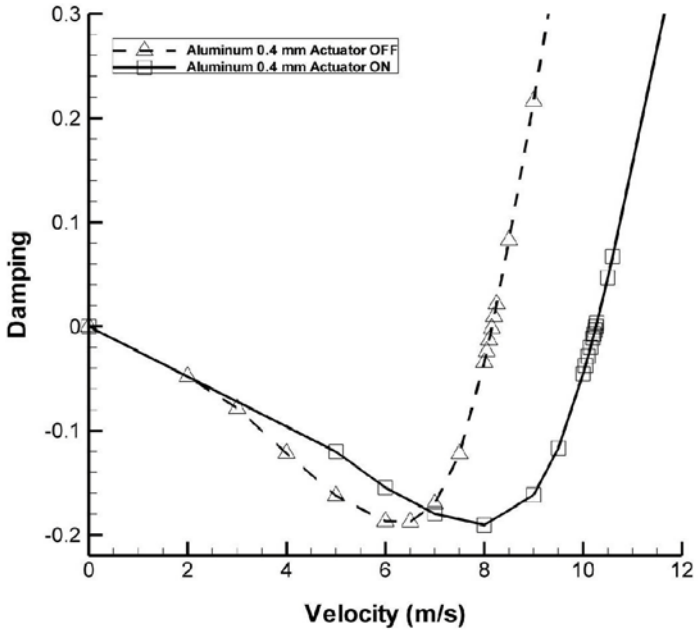

Fig. 31 - Flutter Speed Increment at 250 V.

The use of piezoelectric actuators allows an increment of 20% on flutter speed for a flat thin aluminum plate (Fig. 31). This is a good result since the weight penalty due to the piezoelectric patches is only 1.3%. It should be noted, however, that one is not accounting for the weight of the power supply and wiring that allows the actuation.

Chapter 5 – Conclusions and Future Work

Both passive and active flutter suppression concepts for aeronautical components were studied in this work. Historically, passive flutter solutions have been left behind due to associated increase of weight and loss of performance. Although composite structures have turned the aeroelastic problems even greater due to its flexibility, sandwich structures which ensure higher stiffness combining low-weight cores with high performance material faces are being widely used in aircraft components. It is then conceivable to think that this type of composite may have a contribution in flutter vibration alleviation. Traditional plastic foams like PVC have been used as the core material. However, cork's good anti-vibration and eco-friendly characteristics make it a viable alternative for sandwich structures. The present work intended to compare the flutter behavior of a cork sandwich, and conventional carbon-epoxy and aluminum plates. It has been shown that cork sandwich can provide the same flight envelope for a lighter structure. This is due to the fact that the second moment of area is increased by a thicker structure; however the weight of the structure is not compromised.

Due to the drawbacks of the passive flutter solutions already mentioned, there has been an increasing interest in active flutter suppression concepts. In the present work, an aluminum plate has been modeled with attached piezoelectric patches. These piezoelectric patches exert control over the damping and stiffness properties of the host structure. Using ANSYS® transient analysis, a macro was built in order to actuate the piezoelectric with a fixed voltage but out of phase depending on the oscillation of the plate. This actuation causes a decrease in the oscillation amplitude as if the structure becomes stiffer. Considering an equivalent plate stiffness, the data was exported to ZAERO® in order to compute the increased flutter speed due to actuation. A 20% increase in flutter speed was achieved using a 250 V voltage, the maximum admitted by the piezoelectric patches used in this study. The main goal remains in getting a more efficient plate control without requiring too much power. Having in mind the low strain energy of the current piezoelectric materials, it is conceivable to think that this type of solution will not be applied to aircraft other than small UAV.

It was not the scope of the present work to study the optimal placement of the piezoelectric patches. However, for better and more efficient control purposes, an optimization study should be performed considering the piezoelectric patches location, size, orientation and electrical properties. Also, a control law based on a feedback parameter related to the wing dynamics

should be performed to be tested experimentally using a steady state approach like Single Input Single Output (SISO) or Multi Input Multiple Output (MIMO) controllers.

References

[1]. Fung, Y.C., *An Introduction to the Theory of Aeroelasticity*, Dover Publications, New York, 1993.

[2]. Kehoe, M.W., "A historical overview of flight flutter testing", Dryden Flight Research Center, Edwards, CA, NASA Technical Memorandum 4720, October 1995.

[3]. Bisplinghoff, H., Ashley and Halfman, R., *Aeroelasticity*, Addison-Wesley Publishing Company, 1955, p.272.

[4]. Schwartz, M., Encyclopedia of Smart Materials Volume 1 and Volume 2, John Wiley and Sons, 2002.

[5]. Heeg, J., "Analytical and Experimental Investigation of Flutter Suppression by Piezoelectric Actuation", NASA Technical Paper 3241, March 1993.

[6]. Suleman A., and Costa, A. P., "Adaptive control of an aeroelastic flight vehicle using piezoelectric actuators", Computers and Structures, Volume 82, Issues 17-19, Computational Mechanics in Portugal, 2004

[7]. Costa, T. "Estudo numérico de uma asa com controle active de flutter por realimentação da pressão medida num ponto", PhD Thesis, São Paulo University, São Carlos, 2007.

[8]. Divinycell, *DIAB Sandwich Handbook*.

[9]. Castro, O., "Caracterização de estruturas tipo sandwich com aglomerados de cortiça para aplicação aeroeaspacial", Ms Thesis, Universidade da Beira Interior, Covilhã, 2008.

[10]. Gil, L. "A cortiça como material de construção – Manual Técnico", APCOR, 2007.

[11]. Hodges D. and Pierce G., *Introduction to structural dynamics and aeroelasticity*, Cambridge Aerospace Series 15, Cambridge University Press, New York, 2002.

[12]. Moniz, P. A. A., "Adaptive Aeroelastic Aircraft Structures", PhD Thesis, Instituto Superior Tecnico,. Universidade Técnica de Lisboa, Lisbon, 2005.

[13]. Voracek, D., Pendleton, E., Reichenbach, E., Griffin, K., "Active Aeroelastic Wing Phase I Flight Research Through January 2003", NASA/TM-2003-210741.

[14]. Giurgiutiu, V., “Review of Smart-Materials Actuation Solutions for Aeroelastic and Vibration Control,” Journal of Intelligent Material Systems and Structures, Vol. 11, No. 7, 2000, pp. 525–544.

[15]. C. Rubillo, P. Marzocca, E. Bollt, “Active Aeroelastic Control of Lifting Surfaces via Jet Reaction Limiter Control,” International Journal of Bifurcation and Chaos, Vol. 16, No. 9, 2006, 2559–2574.

[16]. Karagulle, H., Malgaca, L. and ¨Oktem, H.F., “Analysis of Active Vibration Control in Smart Structures by ANSYS®”, Smart Materials and Structures, 13, 661-667, 2004.

[17]. Yaman, Y., Çalışkan, T., Nalbantoğlu V., Waechter, D. Prasad, E., “Active Vibration Control of a Smart Beam”, Proceedings, Canada-US CanSmart Workshop, Smart Materials and Structures, Montreal, Quebec, Canada, Oct. 2001.

[18]. Raja S., Pashilkar, A., Sreedeep, R., and J.V. Kamesh, “Flutter control of a composite plate with piezoelectric multilayered actuators”, Aerospace Sci. Technol. 10 (5) (2006), pp. 435–441.

[19]. Li, L., Yu S., "Active Flutter Suppression Control Using Piezo-Ceramic Actuators", Intelligent Control and Automation. The Sixth World Congress on Vol.2, no., pp.6323-6326, 2006.

[20]. Zhao, H., “Flutter suppression of a high aspect-ratio wing with multiple control surfaces”, Journal of Sound and Vibration, Volume 324, Issues 3-5, 24 July 2009, Pages 490-513, ISSN 0022-460X, DOI: 10.1016/j.jsv.2009.02.026.

[21]. Suresh, S., Kannan N., Sundararajan, N., Saratchandran, P., “Neural Adaptive Control for Vibration Suppression in Composite Fin-Tip of Aircraft”, Int. J. Neural Syst. 18(3): 219-231 (2008)

[22]. Han, J., Tani, J., Qiu J., “Active flutter suppression of a lifting surface using piezoelectric actuation and modern control theory”, Journal of Sound and Vibration, Volume 291, Issues 3-5, 4 April 2006, Pages 706-722, ISSN 0022-460X, DOI: 10.1016/j.jsv.2005.06.029.

[23]. Botez, R., Parvu, P., Doin, A., “Method for Flutter Aeroservoelastic Open Loop Analysis”. CASI Journal, Vol. 49(4), 2003.

[24]. Anderson, E. H., Holcomb, M.D., Bogue, A.X., Russo F.M., “Integrated electro-mechanical devices for active control of vibration and sound.”, Adaptive structures and materials systems symposium, Dallas, Texas, USA; 1997

[25]. Nam, C., Weisshaar, T.A., Kim, Y., "Optimal Sizing and Placement of Piezo Actuators for Active Flutter Suppression," *'95 SPIE Conference on Smart Structures & Materials*, San Diego, CA, Feb. 1995.

[26]. Niezrecki C., Brei, D., and Moskalik, A., “Piezoelectric actuation: state of the art”, *Shock and Vibations. Digest* 33 (4) (2001), pp. 269–280.

[27] Canfield, F., Morgenstern, D., Kunz, D., “Alleviation of buffet induced vibration using piezoelectric actuators”, Computers and Structures 86 pp. 281-291, 2008.

[28]. ZAERO®, Version 4.1, “Applications Manual”, Zona Technology, Eight edition, USA, 2000.

[29]. Razak, N., “Flutter Modeling and Simulation of Wing Section Using Bondgraph Technique”, Ms Thesis, 2005

[30]. Moheimani, S., Fleming, A., *Piezoelectric Transducers for Vibration Control and Damping*, University of Newcastle, Newcastle 2005

[31]. IEEE Standard on Piezoelectricity, IEEE Std. 176, 1978.

[32]. Periasamy, R., “Shape Control of Composite Structures with Optimally Placed Piezoelectic Patches”, Ms Thesis, University of Waterloo, Ontario, 2008.

[33]. Bathe, J., *Finite Element Procedures*, Prentice-Hall, 1996

[34]. ANSYS®, “ANSYS® 5.3 Software Users Guide”, SAS IP, Inc., USA, 1996.

Annex A – ZAERO Input File

```
$ Demonstracao de uma asa em flutter subsonico
$ Solucao dos Métodos K e G.
$
$Begin Executive Control Section
ASSIGN FEM=modo_sand, PRINT=0,FORM=FREE,BOUND=SYM
DIAG 1
CEND
$Begin Case Control Section
TITLE= Flutter Subsonico de uma sandwich de cortiça
ECHO = SORT
SUBCASE = 1
        SUBTITLE=Metodo ZONA6
        LABEL=MACH NUMBER = 0.059, NON-MATCH POINT FLUTTER ANALYSIS
        FLUTTER=100
BEGIN BULK
$
$                 * AERO PARAMETERS / FLIGHT CONDITIONS *
$
$...1..|...2...|...3...|...4...|...5...|...6...|...7...|...8...|...9...|...10..|$
                                                                              $
$
$       ACSID   XZSYM   FLIP    FMMUNIT FMLUNIT REFC    REFB    REFS    +ABC
AEROZ   0       YES     NO      KG      M       0.15    1.0     0.15    +A
$+ABC   REFX    REFY    REFZ
+A      0.0375  0.      0.
$
$       IDMK    MACH    METHOD  IDFLT   SAVE    <--FILENAME-->  PRINT   $
MKAEROZ 80      .059    0       0       SAVE    2DWing_AIC.09   0       +MK1
$       FREQ1   FREQ2   ETC                                             $
+MK1    0.20    0.30    0.35    0.36    0.37    0.38    0.39    0.40    +MK2
+MK2    0.41    0.5     0.6                                             $
$                                                                       $
$                         * WING MACROELEMENT *                         $
$                                                                       $
$       WID     LABEL   ACOORD  NSPAN   NCHORD  LSPAN   ZTAIC   PAFOIL7 $
CAERO7  101     WING    0       7       7                               +CA101
$       XRL     YRL     ZRL     RCH     LRCHD   ATTCHR                  $
+CA101  .0      .0      .0      0.15    0       0                       +CA102
$       XTL     YTL     ZTL     TCH     LTCHD   ATTCHT                  $
+CA102  0.0     0.5     0.0     0.15    0                               $
$                                                                       $
$                    * SURFACE SPLINE FIT ON THE WING *                 $
$                                                                       $
$       EID     MODEL   CP      SETK    SETG    DZ      EPS             $
SPLINE1 100     WING            101     100     0.0                     $
$                                                                       $
$       SETID   MACROID BOX1    BOX2    ETC                             $
PANLST2 101     101     101     THRU    136                             $
$                                                                       $
$       SID     G1      G2      ETC                                     $
SET1    100     1       THRU    213                                     $
$                                                                       $
$                 * NON-MATCHED POINT FLUTTER ANALYSIS *                $
$                                                                       $

$       SETID   SYM     FIX     NMODE   TABDAMP MLIST   CONMLST
FLUTTER 100     SYM     100     0       0
$
$
$...1..|...2...|...3...|...4...|...5...|...6...|...7...|...8...|...9...|...10$
$       SETID   IDMK    DEN     FTMUNIT FTLUNIT VREF    FLUTTF  PRINT   $
FIXMDEN 100     80      1.225   KG      M       1.000           0       +FL1
$       V1      V2      V3      ETC                                     $
+FL1    5.      8.      12.     15.     17.     18.     18.5    19.     +FL2
+FL2    19.2    19.4    19.6    19.7    19.8    19.9    20.     20.2    +FL3
+FL3    20.4    22.     26.                                             $
$                                                                       $
$                         * PLOT AERO MODEL BY PLTAERO *                $
$                                                                       $
PLTAERO 11      YES     0       TECPLOT AERO1.PLT
$                                                                       $
$                                                                       $
$                         * PLOT CP BY PLTCP *                          $
$                                                                       $
PLTCP   3000    SYM     80      6       3       TECPLOT CP1.PLT
$                                                                       $
$                         * PLOT FLUTTER MODE BY PLTFLUT *              $
$                                                                       $
PLTFLUT 10      100     1       1       .3      TECPLOT FLUT1.PLT

PLTMODE 20      SYM     2               .3      TECPLOT MODE2.PLT
PLTMODE 30      SYM     3               .3      TECPLOT MODE3.PLT
$
$                             * V-G PLOT *                              $
$
PLTVG   11      100             V               VG1.PLT
$                                                                       $
ENDDATA
```

Annex B – Matlab Material Conversion Code

```
%PZT BM 500
%Propriedades Mecânicas do PZT
    %Matriz Complicencia (m^2/N)
S11=15.5e-12
S22=S11
S12=-5e-12
S21=S12
S13=-7e-12
S31=S13
S31=S13
S23=S31
S33=19.0e-12
S44=45e-12
S55=45e-12
S66=41e-12
S=[S11 S12 S13 0 0 0;S12 S11 S13 0 0 0;S13 S13 S33 0 0 0;0 0 0 S44 0 0;0 0 0
0 S44 0;0 0 0 0 0 S66]
    %Matriz das Constantes de Deformaçao Piezoeléctrica (C/N)
d31=-175e-12
d32=d31
d33=365e-12
d15=585e-12
d24=d15
d=[0 0 d31;0 0 d31;0 0 d33;0 d15 0;d15 0 0;0 0 0]
d_ansys=[0 0 d31;0 0 d31;0 0 d33;0 0 0;0 d15 0;d15 0 0]
    %Constantes de Voltagem Piezoeléctrica
g31=-11.5e-3
g33=25e-3
    %Constantes Dieléctricas Relativas
e11=1650
e33=1750
e0=8.85e-12   %Permissividade no vácuo
e_perm=[e11 0 0;0 e22 0;0 0 e33]*e0
    %Matriz de Rigidez (N/m^2)
c=inv(S)
    %Alternativa - Introduçao Dados Ortotropicos
EX=1/S11
EY=EX
EZ=1/S33
GXY=1/(2*(S11-S12))
GYZ=1/S44
GXZ=GYZ
NUXY=-S12/S11
NUYZ=-S13/S33
NUXZ=NUYZ
GYZ=1/S44
GXZ=GYZ
    %Matriz Piezoelectrica Tensao
e_ansys=inv(S)*d_ansys
```